AD-A190 389 PHYSICAL FLUID MECHANICS IN MPD THRUSTERS(U) 1/1
MASSACHUSETTS INST OF TECH CAMBRIDGE SPACE SYSTEMS LAB
M MARTINEZ-SANCHEZ 18 SEP 87 AFOSR-TR-87-1760
UNCLASSIFIED AFOSR-86-0119 F/G 21/3 NL

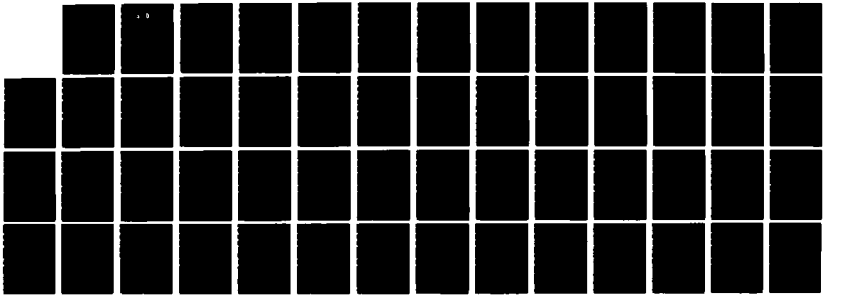

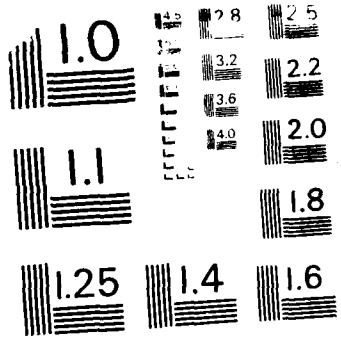

MICROCOPY RESOLUTION TEST CHART
NATIONAL BUREAU OF STANDARDS - 1963

Unclassified

(2)

DOCUMENTATION PAGE

Form Approved OMB No. 0704-0188

AD-A190 309

DTIC ELECTE JAN 19 1988 S D

DTIC FILE COPY

1b RESTRICTIVE MARKINGS

3 DISTRIBUTION/AVAILABILITY OF REPORT
Approved for public release; distribution is unlimited

2b DECLASSIFICATION/DOWNGRADING SCHEDULE

4 PERFORMING ORGANIZATION REPORT NUMBER(S)
MIT, Space Systems Laboratory

5 MONITORING ORGANIZATION REPORT NUMBER(S)
AFOSR-TR- 87-1760

6a NAME OF PERFORMING ORGANIZATION

6b OFFICE SYMBOL (If applicable)

7a NAME OF MONITORING ORGANIZATION
AFOSR/NA

6c ADDRESS (City, State, and ZIP Code)
Cambridge, MA 02139

7b ADDRESS (City, State, and ZIP Code)
Building 410, Bolling AFB DC 20332-6448

8a NAME OF FUNDING/SPONSORING ORGANIZATION
AFOSR/NA

8b OFFICE SYMBOL (If applicable)

9 PROCUREMENT INSTRUMENT IDENTIFICATION NUMBER
AFOSR 86-0119

8c ADDRESS (City, State, and ZIP Code)
Building 410, Bolling AFB DC 20332-6448

10 SOURCE OF FUNDING NUMBERS

PROGRAM ELEMENT NO	PROJECT NO	TASK NO	WORK UNIT ACCESSION NO
61102F	2308	A1	

11 TITLE (Include Security Classification)
(U) Physical Fluid Mechanics in MPD Thrusters (unclassified)

12 PERSONAL AUTHOR(S)
Manuel Martinez-Sanchez

13a TYPE OF REPORT	13b. TIME COVERED	14. DATE OF REPORT (Year, Month, Day)	15. PAGE COUNT
Annual	FROM 5/1/86 TO 4/30/87	9/18/87	45

16 SUPPLEMENTARY NOTATION

17 COSATI CODES		
FIELD	GROUP	SUB-GROUP

18. SUBJECT TERMS (Continue on reverse if necessary and identify by block number)
Electric Propulsion, Plasma Dynamics, MPD Thrusters

19 ABSTRACT (Continue on reverse if necessary and identify by block number)

This report describes work done ~~during~~ the period 5/1/86 - 4/30/87 on three areas of MPD research: (a) A rigorous theoretical examination of the one dimensional flow of a self-field accelerated plasma, clarifying the roles of area change, sonic vs. magnetoacoustic choking, and finite magnetic Reynolds number. (b) Continued development of computational codes for axisymmetric MPD flows, and (c) Results of a first test series on two channels designed to verify predictions on the effects of area variation, showing ability to redistribute current by this means.

20 DISTRIBUTION/AVAILABILITY OF ABSTRACT
☒ UNCLASSIFIED/UNLIMITED ☒ SAME AS RPT ☐ DTIC USERS

21 ABSTRACT SECURITY CLASSIFICATION
Unclassified

22a NAME OF RESPONSIBLE INDIVIDUAL	22b TELEPHONE (Include Area Code)	22c OFFICE SYMBOL
Dr Mithat Birkan	(202) 767-4937	AFOSR/NA

DD Form 1473, JUN 86 Previous editions are obsolete.

SECURITY CLASSIFICATION OF THIS PAGE
Unclassified

SPACE SYSTEMS LABORATORY

Department of Aeronautics and Astronautics

Massachusetts Institute of Technology

Cambridge, Massachusetts 02139

Physical Fluid Mechanics in MPD Thrusters

Annual Report for the period 5/1/86 - 4/30/87

on Grant AFOSR - 86-0119

Attn: Mithat Birkan AFOSR/NA

Bolling AFB

Washington, D.C. 20332

by Manuel Martinez-Sanchez, Associate Professor

MIT, Department of Aeronautics and Astronautics

9/18/87

1. Abstract

This report describes work done during the period 5/1/86 - 4/30/87 on three areas of MPD research: (a) A rigorous theoretical examination of the one-dimensional flow of a self-field accelerated plasma, clarifying the roles of area change, sonic vs. magnetoacoustic choking and finite magnetic Reynolds number. (b) Continued development of computational codes for axisymmetric MPD flows, and (c) Results of a first test series on two channels designed to verify predictions on the effects of area variation, showing ability to redistribute current by this means.

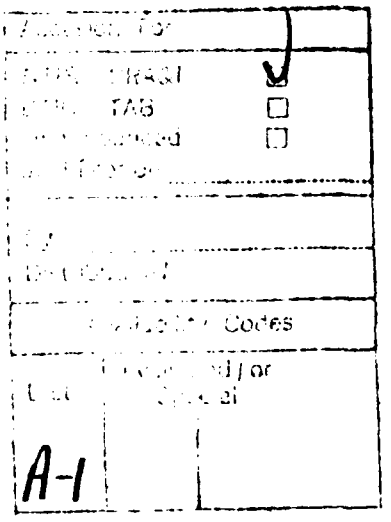

1. Introduction . Research Objectives

Our work statement for the period covered by this Report on AFOSR 83--0035-C included both theoretical and experimental tasks. In summary, these were as follows:

(a1) Refinement of analytical models. Use of singular perturbation methods to connect the high interaction bulk plasma to wall regions. Non-equilibrium effects.

(a2) Numerical simulation of Self-Field MPD Flows. To refine previously developed fluid dynamic codes and to use them in studying various parametric effects.

(a3) Extension of the Above to Applied Field MPD Flows. Confined to axisymmetric conditions, with no current spokes.

(b1) Experimental Study of Various Trhuster Configurations. The aim here was to validate theoretical concepts developed previously about the effects of electrode contouring.

(b2) Diagnostics Development. To apply previously acquired optical and signed processing equipment for the measurement of various plasma parameters in connection with (b1) above.

In the following sections we give an overview of the accomplishments in these tasks and of the occasional departures from the original plan. Reference will be made to three papers presented by our group at the 1987 International EP Conference, where the details of most of the work were described. These papers are included here as Appendices.

2. Outline of Work Accomplished

2.1 Theory In our efforts to clarify the dynamics of self-field accelerated MPD flows, we had previously developed the limiting concept of a high Magnetic Reynolds Number (Rm) plasma (1), which was useful in understanding the close connection between flow area variation and distribution of current along the

length of an MPD thruster of slender geometry, and also made clear the dominant role of magnetoacoustic waves and magnetoacoustic choking phenomena.

The practical range of Rm is from 2 to 10 or so, which is not extremely high, and it was not entirely clear to what extent these "high Rm" results would apply to realistic conditions. Particularly troublesome to some colleagues was the fact that in this limit, thermal effects were relegated to a definitely secondary role, with, for instance, no mention of the delicate balance required at a sonic point, as had been discussed by several previous authors (2), (3). In fact, these sonic conditions were thought to be entirely responsible for the determination of the all-important channel voltage for a given current (2), and, following this, for the occurrence of conditions, at high values of $(\text{current})^2/(\text{mass flow rate})$, where the back emf exceeded locally the channel voltage, a condition that was identified as leading to the symptoms known as "onset" (3).

We were also aware, as was pointed out in Ref. (1), that the approximations leading to the simple behavior of the "high Rm" plasma would break down in regions of high current concentration, near the inlet and exit of a channel. However, the proper way to account for these regions was not known prior to the work reported here. Even at this time, the complications brought about by the simultaneous effects of high magnetic Reynolds number and high Hall parameter in two or three-dimensional geometries are not well understood. For example, each of these two effects contributes to the existence of a current concentration at the root of the cathode, while the Hall effect alleviates the corresponding high Rm concentration at the anode root. While these factors are separately understood now, no simple theory of the combined effect exists yet. In view of the difficulties mentioned above, which were severe even with no Hall currents (as in a one-dimensional channel with segmented electrodes in a Faraday connection), we decided to postpone work on multi-dimensional formulations and concentrate our efforts on a precise analysis of the one-dimensional case. The results of this work reported in Ref. (4), which is included here as Appendix 1.

The key result is that even as $Rm \to \infty$, the effects of magnetic diffusion (i.e., ohmic dissipation) are to be retained in ever thinner inlet and exit layers, in order to satisfy the boundary conditions on the magnetic field (for the prescribed current). This is entirely analogous to the classical very thin viscous boundary layers in nearly inviscid fluids. And, also in analogy to boundary layer theory, the effects of such layers may be important for some purposes (as for drag in the viscous case) while they may be ignored for others (as for lift). In the MPD case, we show in Appendix 1 how the existence of these sharp inlet and exit current layers, where dissipation concentrates, is of minor consequence for voltage prediction, but strongly affects calculations of dissipation (hence efficiency and thrust). It is also shown that sonic passsage does occur within the inlet layer, and that proper satisfaction of the smooth sonic passage conditions is indeed essential if this layer is to be resolved properly. However, the major flow metering function is still found to be fulfilled by magneto-sonic choking at a channel throat, well downstream of the sonic point.

In addition to clarifying these points and hence for the first time providinng a corrct solution for high Rm, the work reported in App. 1 explored numerically the range of validity of the $Rm \to \infty$ solution. It was found that, for channels that are contoured so as to evenly distribute the current (which leads to increased efficiency and reduced electrode stress), the high Rm results hold well for Rm down to about 3 or so, and depart only gradually at lower Rm. In

contrast, in constant-area channels, the strong dissipation near the exit at finite Rm produces positive pressure gradients that slow the flow and reduce the local magnetic convection, leading to thermal choking at Rm≈5, to embedded shocks between Rm≈5 and Rm≈2, and to subsonic flow at lower Rm. These regimes had been previously reported by King (2). Thus, high Rm predictions for constant-area cases are of limited validity for Rm $\lesssim$8. On the other hand, constant area channels are probably impractical due to the strong current concentrations and the attendant reduction in thrust efficiency.

Finally, we compared the voltage and thrust predictions of our models (with finite Rm) to those reported by the Princeton group (5) for an experimental slender channel, and found good agreement in both cases, including a good account of the transition between the electrothermal and electromagnetic regimes.

2.2 Numerical Simulation. Preliminary results of a developmental axisymmetric MPD flow numerical model were included in our previous yearly report (6). This work has been continued and refined, with the most recent results being discussed in Ref. 7 and in our Appendix 2.

The refinements have been motivated by numerical difficulties encountered at the higher current levels, for a given flow rate. They have included a smoother, numerically generated curvilinear grid (see Fig. 1 of App. 2) with concentrations near corners and walls, as well as a more rigorously calculated Jacobian matrix, including both, flow and electromagnetic equations. The Jacobian matrix is the matrix of partial derivatives of the various governing

equations w.r.t. the chosen dependent variables, evaluated at all the grid points, and is used, after inversion, to generate a new linearized solution to all the equationns. These are re-linearized and the process is iterated. It has been found that this Newton-Raphson method converges very rapidly (4-6 iterations, compared to thousands of time steps in most time-marching schemes), but requires large amounts of computer storage. This means that the grid resolution must necessarily be limited, for any given machine capacity. We are currently working with 20 x 50 grids in our Micro-Vax computer. This relatively coarse grid, coupled with the very steep property gradients found in certain regions of the solution, leads to the occurrence of numerical fluctuations which necessitate an objectionable amount of artificial numerical damping, and which, at high currents, induce negative density "pockets", followed by generalized breakdown of the solution. It must be also stated that the stability limits of the Newton-Raphson algorithm for the kind of mixed convective-diffusive and elliptic-hyperbolic type of equations we are using are not known at present, and hence other factors may be at work in limiting the method.

Within these limitations, the results obtained for 6 g/sec of Argon at currents to 10 KA are quite interesting (see Appendix 2). The strong plasma density concentration at the cathode tip (plasma focus) is clearly indicated in Fig. 6 of App. 2, as is the existence of rarefied regions near the anode lip and at the cathode shoulder. The cathode tip and root current concentrations, well known to experimenters, are visible in Fig. 3 of App. 2.

Incidentally, the numerical instability appears to be unrelated, at least in principle, to the expected anode depletion at high $I^2/\dot{m}$, since the plasma density over most of the cathode is only some 20% lower than that at the cathode at I = 10 KA, and is well above that level required to supply the local random electron flux to the anode wall.

Work is underway now to exploit the larger capabilities of a multiprocessor vectorized computer, of which partial ownership was acquired by a special AFOSR supplementary grant. Two lines of attack are planned: (a) to explore the behavior of the Newton-Raphson code with finer grids and (b) to utilize sophisticated time-marching techniques (Flux-Corrected Transport Codes), now available in our VAX. The latter work will be undertaken by a new doctoral student, Mr. Eli Niewood who is supported by an NSF fellowship, while the Newton-Raphson work will be continued by Mr. J. Marc Chanty.

The slower than expected development of our numerical work has forced us to postpone consideration of applied-field cases. This is still contemplated for the future, since no essential new difficulties are expected once the self-field case is better in hand (with the exception of spoke generation, which would require some form of 3-D calculation).

2.3 Experimental Work. In cooperation with Dr. Peter Turchi and collaborators of the Washington office of R & D Associates, we have designed, built and tested several MPD channels in order to learn about the degree of fidelity of the necessarily simplified theories we have developed previously. This work was largely carried out by doctoral candidate D. Heimerdinger, who spent several months at the R&D lab. in the course of the development of the required experimental apparatus and facilities. He was also helped by a second graduate student, Mr. D. Kilfoyle wo installed the optical diagnositcs and participated in the experiments themselves.

The preliminary results of tests with two channels, one of constant area and one featuring a divergent section, are reported in Ref. 8 which is also reproduced in Appendix 3. Additional results with a convergent-divergent channel will be reported later, together with a more complete analysis of the data presented here.

The tests are pulsed (0.5 msec), allowing a relatively simple apparatus. In an attempt to avoid the complicating efforts of axial symmetry, the channels were built with a fairly large cathode radius and small cathode-anode gap, thus approaching two dimensionality. This also has the effect of boosting the level of current that can be passed before "onset". On the other hand, it also leads to weakened electric and magnetic fields for a given total current, and, on the initial test series, some difficulty was encountered to obtain smooth, symmetric discharges at the design conditions.

What apeared to be symmetric discharge conditions (as determined by sub-microsecond frontally taken photographs) were finally obtained by a combination of increasing the current, decreasing the flow rate, and simply accumulating over one hundred pulses in order to condition the electrode surfaces by burning away the inevitable adsorbed and oxydized layers. The conditions obtained this way, which are those reported in App. 3, were well above the theoretically expected onset, but during the test series with the constant area channel we did not encounter the MHz voltage fluctuations which have come to be regarded as the signature of onset. Upon examination of the channel at the end of the tests, it was clear that large arcs had been present on both anode and cathode, and they were visible in some of the high-speed photographs taken during the tests. It was only later that we have been able to show conclusively that onset was indeed exceeded in these tests, and this has come mainly from monitoring the near-anode voltage drops in a subsequent test series (results to be reported later). The absence of voltage "hash" in the constant-area channel which initially misled us into believing we were still below onset, has been seen to be a peculiarity of this geometry, despite other clear evidence of anode depletion. The contoured channels do exhibit voltage "hash", although with some delay and with individually differentiated patterns.

Given the fact that conditions during the tests reported here were above onset, we cannot expect to find good correlation with theoretical results that are for smooth, non-depleted operation. There are, however, clear indications of the main effect that was pursued, namely, a significant redistribution of current due to the exit flaring in the second channel, in the sense of reducing the strong exit concentration measured in the constant-area channel (see Fig. 13 of App. 3).

As indicated before, diagnostics development has proceeded in parallel with the rest of the experimental program, and spatially and spectrally resolved data of the near-exit plume were obtained during some of the tests. Additional measurements were made using an R&D plasma generator. These results are not given here in detail, however, since their interpretation is incomplete at the reporting time. We will simply note that we use a fast digitizing Silicon Intensified Target (SIT) camera, together with a 1.26 m. Czerny-Turner spectroscope, to obtain at once complete transverse profiles of the plane, with the spectrum either resolved over a region containing several H lines for Te measurements, or containing the resolved Hβ line for Stark measurement of n_e. Measurement of T_i by Doppler broadening is also attempted. An algorithm for automatic Abel inversion of the data has been developed, which uses FFT spectral methods, allowing pre-filtering of the generally noisy data.

3. Personnel Associated with this Research

The work was directed by Associate Professor Manuel Martinez-Sanchez, with the cooperation of Graduate Research Assistants D. Heimerdinger (Doctoral Candidate), J. March Chanty (Doctoral Candidate), D. Kilfoyle (M.S. Candidate) and Eric Sheppard (Doctoral Candidate).

4. References

1. M. Martinez-Sanchez and D. Heimerdinger "Two-dimensional Analysis of an MPD Arcjet". AIAA paper 85-2040, presented at the 18th International Electric Propulsion Conference, Alexandria, Virginia, October 1985.

2. King, D.Q. "Magnetoplasmadynamic channel flow for design of coaxial MPD thrusters". Ph.D. Dissertation, Princeton University, Princeton, N.J. 1981.

3. J.L. Lawless and V.V. Subramamian. "Theory of Onset in Magnetoplasmadynamic Thrusters". J. Propulsion, Vol. 3, No. 2, pp. 121-127 March-April 1987.

4. M. Martinez-Sanchez. "The Structure of Self-Field Accelerated Plasma Flows". Paper AIAA-87-1065, Presented at the 19th International Electric Propulsion Conference, Colorado Springs, Colorado, May 1987.

5. R.G. Jahn and A.J. Kelly, "Megawatt Level Electric Propulsion Perspectives". Presented at the Open Sessions of the 4th Syposium on Space Nuclear Power Systems, Alburquerque, New Mexico, January 1987.

6. M. Martinez-Sanchez, "Performance-Limiting Factors in MPD Trhusters". Final Report on Grant AFOSR-83-0035-C, for the period 12/15/84-4/30/86.

7. J.M.G. Chanty and M. Martinez-Sanchez, "Two-Dimensional Numerical Simulation of MPD Flows". Paper AAIA-871090, presented at the 19th International Electric Propulsion Conference, Colorado Springs, Colorado, May 1987.

8. D.J. Heimerdinger, M. Martinez-Sanchez, J.F. Davis and P.J. Turchi, "Effect of Axial Variation of Electrode Spacing on MPD Arcjet Behavior". Paper AIAA 87-0998, presented at the 19th International Electric Propulsion Conference, Colorado springs, Colorado, May 1987.

APPENDIX I

AIAA-87-1065

The Structure of Self-Field Accelerated Plasma Flows

M. Martinez-Sanchez,
Massachusetts Institute of Technology,
Cambridge, MA

AIAA/DGLR/JSASS 19th International Electric Propulsion Conference
May 11-13, 1987
Colorado Springs, Colorado

THE STRUCTURE OF SELF-FIELD ACCELERATED PLASMA FLOWS

By Manuel Martinez-Sanchez

M.I.T., Dept. of Aeronautics & Astronautics

Abstract

An analysis is presented of self-field accelerated quasi-one-dimensional plasmma flows with zero axial current. The dominance of magnetic convection over diffusion leads to the formation of inlet and exit conncentration layers which are analyzed by asymptotic matching. The sonic passage condition is found to control injector conditions, but not channel voltage. Throats are shown to be approximately magnetosonic. Performance factors accounting for inlet convergence and nozzle divergence are derived by exploiting the smallness of pressure forces. The effect of finite magnetic Reynolds nuumbers is seen to be moderate down to $Rm = 3$ for conntoured channels, but to $Rm = 10$ for constant-area channels. Contouring is shown to be effective for control of current and dissipation concentrations.

1. Introduction This work is an attempt to clarify the roles of various fluid and electromagnetic effects on determining the performance and the distributions of current and density in MPD self-field thrusters. The general problem, with all its atomic physics implications and with due account for real electrode effects, is clearly beyond simple analysis, and must be tackled by a combination of experiment and numerical simulation. However, even the idealized flow problem, where only minimal physics is included, has so far eluded analysis to a large extent. Since even at the simplest meaningful level of abstraction (i.e., quasi-one dimensional channel flow) the fluid mechanics of a self-field accelerated plasma is complex and unfamiliar, it is worthwhile to go through its analysis in as complete a fashion as possible. The results will shed light on several aspects of MPD operation, including the role of thermal choking in determining thruster voltage[1], the possibility of the back e.m.f. exceeding the applied voltage[2] the role of channel contouring[3] and the usefulness of the large Magnetic Reynolds number approximation,[3] as well as the low gas pressure approximation, both of which could be exploited in multi-dimensional modeling work.

2. Formulation We wish to postulate conditions under which a quasi-one dimensional flow model is tenable. For a low-pressure partially magnetized flow as in self-field MPD, this is complicated by the Hall effect, which, for equipotential walls, produces substantial axial currents and subsequent transverse density gradients, leading eventually to depletion of the anodic region.[4,5,6]

*This work was supported by the Air Force Office of Scientific Research under Grant No. AFOSR-86-01190

Associate Professor, Dept. Aeronautics and Astronautics,
Member AIAA

Conceptually, at least two approaches can be taken to bypass this problem: (a) assume a high enough power level that the Hall effect becomes negligible, or (b) assume an appropriate axial electrical field can be imposed through segmentation, such as to cancel the axial (Hall) current. Option (a) exists because the Hall parameter, β, can be shown to scale as $I/\dot{m}$ for a given fluid and geometry, while Baksht's theory indicates that, at the initial (onset) condition $\dot{m} \propto I^{3/4}$, or, assuming operation near onset, $\beta \propto 1/\sqrt{I}$. Option (b) allows uniform transverse conditions even in the presence of a finite Hall effect, and will be assumed in this work. The required E_x axial field can be found a-posteriori, and no attempt will be made here to discuss implementation of the implied segmented construction, other than to point out that the fields involved are typically of the order of 5-20 V/cm and should pose no axial breakdown problems.

The steady-state quasi-one dimensional equations of mass and inviscid momentum conservation, written in terms of cross-section averaged properties, are

$$\rho u A = \dot{m} \tag{1}$$

$$\rho u \frac{du}{dx} + \frac{d}{dx}\left(p + \frac{B^2}{2\mu_0}\right) = 0 \tag{2}$$

where B is the magnitude of the self-induced magnetic field, which is perpendicular to the centerline direction. The total enthalpy conservation law is

$$\rho u \frac{d}{dx}\left(h + \frac{u^2}{2}\right) = \vec{E} \cdot \vec{J} \tag{3}$$

where the average current density $\vec{J}$ is, by assumption, purely transverse and is related to the magnetic field by

$$J = -\frac{1}{\mu_0}\frac{dB}{dx} \tag{4}$$

The condition $\nabla \times \vec{E} = 0$ can be shown to reduce in our case of zero axial current to

$$\frac{d}{dx}(E_y H) = 0 \; ; \; E_y H = V_y = \text{const.} \tag{5}$$

which is the same as would apply in the absence of Hall effect. Here, H is the inter-electrode channel height. There is, however, a non-zero axial field given (on average) by

$$E_x = \beta (E_y - uB) \tag{6}$$

where β is the Hall parameter.

Under these conditions, the mean electrical work $\vec{E} \cdot \vec{J}$ becomes

$$\vec{E} \cdot \vec{J} = -\frac{1}{\mu_0} E_y \frac{dB}{dx} \tag{7}$$

and the energy equation (Eq. (3)), combined with Eqs. (5) and (7), integrates to

$$\dot{m}(h + \frac{u^2}{2}) + \frac{W}{\mu_0} V_y B = \text{const.} \qquad (8)$$

where W is the channel width, which is assumed constant. Note that this is also the same form that would apply with zero Hall effect.

To complete the formulation, the transverse component of Ohm's law (neglecting electron diffusion effects) is

$$j = \sigma(E_y - uB) \qquad (9)$$

where σ is the scalar conductivity. Also, an equation of state is needed, most usefully in the form $h = h(P,\rho)$. In this work we will use either a simple perfect gas model, with constant ratio of specific heats, or an ionization equilibrium model for a noble gas.

In our analysis we will take the point of view of having a prescribed total current I (implying a given $B_0 = \mu_0 I/W$) and flow rate $\dot{m}$, with a geometrical throat of area A^*. Also given is the inlet total enthalpy, $h_{to} = h_o + \frac{1}{2}u_o^2$. The voltage Vy (or the field E_y at some section) is then to be determined. Also unknown are the inlet density and velocity (but not their product, since $\dot{m} = \rho_o u_o A_o$ is known). As to exit conditions, there are two logical alternatives: (a) Since the exit velocity is likely to be higher than the speed of propagation of flow disturbances (i.e., as we will see, the magnetoacoustics speed), we can leave exit conditions unspecified, in the understanding that complete expansion to zero magnetic field and pressure will occur external to the channel. (b) In the context of a quasi-one dimensional model, we can "bottle up" this external expansion by imposing, somewhat artificially, zero magnetic field at the exit plane. This procedure will increase the concentration of current in the exit region, and will thus lead to stronger Ohmic losses and an underestimation of efficiency, but it has the advantage of providing simple and consistent estimates of overall performance without the need for two or three-dimensional external flow calculations.

It is convenient to no non-dimensionalize variables using reference values derived from the prescribed quantities. These reference quantities are:

$$B_{ref} = B_0 \qquad u_{ref} = \frac{B_0^2 A^*}{2\mu_0 \dot{m}} \qquad p_{ref} = \frac{B_0^2}{2\mu_0}$$

$$\rho_{ref} = \frac{p_{ref}}{u_{ref}^2} = \frac{2\mu_0}{B_0^2}\left(\frac{\dot{m}}{A^*}\right)^2 \qquad h_{ref} = u_{ref}^2$$

$$E_{ref} = u_{ref} B = \frac{B_0^3}{2\mu_0 \dot{m}} \qquad j_{ref} = \frac{B_0}{\mu_0 L}$$

$$A_{ref} = A^* \qquad x_{ref} = L \qquad V_{ref} = E_{ref} H^* \qquad (10)$$

An important non-dimensional parameter is the Magnetic Reynolds number, $Rm = \mu_0 \sigma u_{ref} L$. Its inverse,

$$\varepsilon = \frac{2\dot{m}}{\sigma \mu_0 L A^* B_0^2} \qquad (11)$$

is numerically in the range 0.1-0.3 for realistic Magneto Plasmadynamic (MPD) thrusters.

In what follows, we will work with the non-dimensional variables

$$b = B/B_0 \quad , \quad \bar{u} = u/u_{ref} \quad , \quad \bar{p} = p/p_{ref}$$

$$\bar{\rho} = \rho/\rho_{ref} \quad , \quad \bar{h} = h/h_{ref} \quad , \quad \bar{E} = E_y/E_{ref}$$

$$J = j/j_{ref} \quad , \quad a = A/A^* = H/H^* \quad , \quad \xi = x/L$$

$$\bar{V} = V_y/V_{ref} \qquad (12)$$

In terms of these variables, the governing equations become

$$\bar{\rho}\bar{u}a = 1 \qquad (13)$$

$$\bar{\rho}\bar{u}\frac{d\bar{u}}{d\xi} + \frac{d}{d\xi}(\bar{p} + b^2) = 0 \qquad (14)$$

$$\bar{\rho}\,\bar{u}\frac{d\bar{h}}{d\xi} - \bar{u}\frac{d\bar{p}}{d\xi} = 2\varepsilon J^2 \quad ; \quad \bar{h} = \bar{h}(\bar{p},\bar{\rho}) \qquad (15)$$

$$\varepsilon J = \bar{E} - \bar{u}b \qquad (16)$$

$$J = -\frac{db}{d\xi} \qquad (17)$$

$$\bar{E}a = \bar{V} \qquad (18)$$

Notice that Eq. (15) is the internal energy equation, obtainable by subtracting the product of u times Eq. (2) from the differential form of Eq. (8). Clearly, the alternative is the non-dimensional form of Eq. (8) itself:

$$\bar{h} + \frac{\bar{u}^2}{2} + 2\bar{V}b = \bar{h}_{to} + 2\bar{V} \qquad (19)$$

where $\bar{h}_{to} = \bar{h}_o + \frac{1}{2}\bar{u}_o^2$

Since $J = -db/d\xi$, the small parameter ε is seen to multiply magnetic field derivatives. In the limit as $\varepsilon \to 0$ the system (13)-(18) is therefore singular, with possible layers of rapidly varying properties at the channel's inlet and exit, due to the presence of prescribed boundary conditions there, and with the body of the channel, between such layers, constituting what mathematically speaking would be called the "outer" region, in which the ε terms are insignificant.

3. Singular Perturbation Problem - The Zero'th Order Solution - In the limit when $\varepsilon \to 0$, the width of the singular "inner" layers near $\xi = 0$ and $\xi = 1$ tends to zero, and for nearly the whole length of the channel, Eqs. (15) and (16) reduce to

$$\frac{d\bar{h}^0}{d\xi} = \frac{1}{\bar{\rho}^0}\frac{d\bar{p}^0}{d\xi} \qquad (20)$$

$$\bar{E}^0 = \bar{u}^0 b \qquad (21)$$

Here the superscript $(^0)$ refers to the "outer" solution. Eq. (20) indicates isentropic flow in this region. Eq. (21), combined with $\bar{E}^0 a = \bar{V}$ and $\bar{\rho}^0 \bar{u}^0 a = 1$, gives

$$\frac{b}{\bar{\rho}} = \text{const.} = \bar{E}^0 a = \bar{V} \qquad (22)$$

where $\bar{V}$ is the (non-dimensional) channel voltage to order zero. Notice that this voltage is the same throughout the channel, including the singular "inner" layers, but may include higher order perturbation terms for non-zero ε.

The nature of the zero'th order "outer" solution can be readily seen by defining an equivalent pressure which includes both gas and magnetic contributions

$$\Pi = \bar{p} + b^2 \qquad (23)$$

In terms of Π, the equation of motion (to any order) is $\rho d\bar{u} + d\Pi = 0$, and since in this zero'th order outer solution both $\bar{p}$ and $\bar{b}$ have been found to depend on $\bar{\rho}$ alone, the flow is barotropic and behaves the same way as an ordinary ideal gas flow with a special pressure-density relationship. In MPD flows $b^2 >> p$, so that, to a first approximation, $\Pi \sim \rho^2$, and the effective "γ" of the flow is about 2. The speed of propagation of small disturbances in such a flow is (in non-dimensional terms)

$$\bar{c} = \sqrt{\frac{d\Pi}{d\bar{\rho}}} = \sqrt{\frac{d\bar{p}}{d\bar{\rho}} + \left(\frac{\bar{b}}{\bar{\rho}}\right)\frac{d\bar{b}^2}{d\bar{\rho}}} = \sqrt{(\bar{c}_s)^2 + 2\bar{V}^2\bar{\rho}^0} \qquad (24)$$

where c_s is the ordinary speed of sound, and $2\bar{V}^2\bar{\rho}^0 = 2\frac{b^2}{\rho}$ can be identified as the square of the Alfven velocity, and is, in fact, the dominant contribution to Eq. (26). It is a known property of ideal gas flow that the gas velocity at a throat must equal the small-disturbance propagation velocity, provided the downstream pressure is low enough. Therefore, we deduce the existence of a magnetosonic flow choking condition, which, for a prescribed flow rate and throat area, must imply a certain relationship among the upstream conditions. In our problem "upstream" conditions must be those immediately past the thin inlet layer, through which we can have nearly discontinuous variations. Let us denote this location by a subscript (1), to distinguish it from inlet conditions (subscript (o)). Since $\bar{\rho}_1$ can be found from the continuity equation and $\bar{h}_1^0$ depends on $\bar{\rho}_1$ and ρ_1, the remaining independent variables at (1) are $\bar{\rho}_1$, b_1^0 and $\bar{u}_1^0$. In addition, the voltage $\bar{V}$ is still an unknown. The condition that the throat be magnetosonic is then of the form $F(\bar{\rho}_1^0, b_1^0, \bar{u}_1^0; \bar{V}) = 0$, the specific details depending on the fluid model adopted.

Additional equations for $\bar{\rho}_1^0, b_1^0, \bar{u}_1^0$ and $\bar{V}$ can be found by asymptotic matching of the "outer" solution so far discussed to the "inner" solution through the inlet layer. Since the thickness of this layer is of order ε, we can, in the zero'th approximation, ignore area variation in it; on the other hand, the ε terms in Eqs. (15) and (16) are now to be retained. It is convenient to re-scale distance by defining an inner coordinate

$$\xi_1 = x/\varepsilon \qquad (25)$$

The "inner" equations of momentum, total energy and Ampere's law follow from (14), (19) and (16) respectively:

$$\frac{1}{a_0}\frac{d\bar{u}^1}{d\xi_1} + \frac{d}{d\xi_1}(\bar{p}^1 + b^{1^2}) = 0 \qquad (26)$$

$$\bar{h}^1 + \frac{\bar{u}^{1^2}}{2} + 2\bar{V}b^1 = \bar{h}_{to} + 2\bar{V} \qquad (27)$$

$$\frac{db^1}{d\xi_1} = -\left(\frac{\bar{V}}{a_0} - \bar{u}^1 b^1\right) \; ; \; \bar{E}^1 = \frac{\bar{V}}{a_0} \qquad (28)$$

Initial conditions for the equations can be applied at inlet, as has been done in (27) ($b^1(o) = 1$, $(\bar{h}^1 + u^{1^2}/2) = \bar{h}_{to}$). The inlet velocity $u^1(o) = \bar{u}_0$ and pressure $\bar{p}^1(o) = \bar{p}_0$ are not a-priori known, however.

Eq. (26) integrates to

$$\bar{u}^1 = \bar{u}_0 + a_0\left[(\bar{p}_0 - \bar{p}^1) + 1 - b^{1^2}\right] \qquad (29)$$

Two equations for the conditions at (1) can be simply found by expressing the integrated inner laws (27) and (29) at their outer limits:

$$\bar{u}_1^0 = \bar{u}_0 + a_0\left[\bar{p}_0 - \bar{p}_1^0 + 1 - b_1^{0^2}\right] \qquad (30)$$

$$\bar{h}_1^0 + 1/2(\bar{u}_1^0)^2 + 2\bar{V}b_1^0 = \bar{h}_{to} + 2\bar{V} \qquad (31)$$

An additional matching condition can be obtained from Eq. (28): since b^1 must smoothly tend to b_1^0 as the inner variable ξ_1 tends to infinity, we must have

$$\bar{V} = a_0 \bar{u}_1^0 b_1^0 \qquad (32)$$

This is in fact, equivalent to Eq. (21), when expressed at the initial point of the outer range.

It can be seen now that Eqs. (30), (31) and (32), plus the magnetosonic choking condition, will determine properties at (1) and voltage $\bar{V}$ provided the inlet velocity is known (the inlet pressure $\bar{p}_0$ would then follow from the given $\bar{\rho}_0 \bar{u}_0$ and $\bar{h}_{to}$). This indicates that some additional condition remains to be found, and this will be seen to be the smooth passage through the sonic point (which occurs well upstream of the magnetosonic point, in fact, within the inlet layer). The importance of this condition has been emphasized by King[7] and Lawless and Subramanian [8] who state that it is the sonic passage condition that governs the channel voltage. On physical grounds, this would seem unlikely (in fact, Ref. (3) speaks of a "non-intuitive result"). Indeed, the voltage is largely the induced back e.m.f., determined by the eventual gas velocity, which is many times larger than the speed of sound, and one would expect downstream conditions to play the major role in determining $\bar{V}$. That this is the case can be seen from the discussion so far: the initial velocity $\bar{u}_0$ is a very small quantity (of order 0.01, as our results will show) and its direct contribution to Eqs. (30) and (31) can be safely ignored. On the other hand, since $\bar{\rho}_0 \bar{u}_0 a_0 = 1$, setting $\bar{u}_0 = 0$ would imply an infinite density, and hence pressure $\bar{p}_0$; in fact, the small, but non-zero $\bar{u}_0$ leads to a rather large $\bar{\rho}_0$, but still to a small $\bar{p}_0$ (of order 0.1) as corresponds to the physical regime of operation of MPD devices (gas pressure << magnetic pressure). It follows that both $\bar{u}_0$ and $\bar{p}_0$ could be ignored (and hence also $\bar{h}_{to}$) in Eqs. (30) and (31), and $\bar{V}$ could be calculated to a fair approximation with no reference to any gas thermodynamics, and no need for a sonic passage condition. As we will explicitly show in a simple case, the role of this sonic passage condition is mostly to determine the precise value of the inlet variables ($\bar{\rho}_0$, $\bar{u}_0$, etc.) once the voltage $\bar{V}$ is known from the downstream conditions.

The form of the sonic passage condition can be seen for instance by solving the set of equations (13) to (17) for the individual derivatives. This will in fact be useful for later numerical computations. For the velocity derivative, we obtain

$$(\bar{u}^2-\bar{c}_s^2)\frac{d\bar{u}}{d\bar{\xi}} = \bar{u}\bar{c}_s^2\frac{d\ln a}{d\bar{\xi}} - \frac{2}{\varepsilon\bar{b}}(\bar{E}-\bar{u}\bar{b})\frac{\bar{E}-K\bar{u}\bar{b}}{K-1} \qquad (33)$$

where $\bar{c}_s = \sqrt{\frac{\partial\bar{p}}{\partial\bar{\rho}}}$ is the normalized isentropic speed of sound, and

$$K = \bar{\rho}\left(\frac{\partial\bar{h}}{\partial\bar{p}}\right)_{\bar{\rho}} \qquad (34)$$

is a thermodynamic quantity which reduces to $\gamma/(\gamma-1)$ in the case of an ideal gas with constant specific heat ratio γ. It is clear that when $\bar{u} = \bar{c}_s$, the whole right hand side of Eq. (33) must be simultaneously zero. In the present zero'th order approximation ($\varepsilon \ll 1$), only the second term is of concern (which is equivalent to ignoring area variation in the "inner" region). The two roots of this second term are $\bar{E} = \bar{u}\bar{b}$ and $\bar{E} = K\bar{u}\bar{b}$, and the first of these is reached at the outer edge of the initial layer. Since $\bar{u}\bar{b}$ increases from near zero, and $K>1$, the condition

$$\bar{E}_s = (K\bar{u}\bar{b})_s \qquad (35)$$

is reached inside the layer, and must be the sonic passage condition. Here the subscript s indicates the sonic point. Together with $\bar{u}_s = \bar{c}_s$ and with the conservation equations expressed at the sonic point (Eq. (27), (29)), this allows elimination of all variables at s, yielding the final required equation for the calculation of all properties at stations (o) and (1) and of the voltage $\bar{J}$.

Once these values are known, channel exit conditions must be calculated by solving a second set of "inner" equations similar to Eqs. (26)-(28) for the rapid variations that occur near the channel exit, where the condition $\bar{b} = 0$ is to be imposed. The task is now simple, since the eigenvalues of the problem, i.e., $\bar{V}$ and $\bar{u}_o$ are by this time known quantities; physically, if the exit speed is greater than (or equal to) the magnetosonic speed, exit conditions cannot influence upstream conditions. We thus can calculate exit velocity, and hence thrust, efficiency and specific impulse of the thruster at the specified current and mass flow.

The thrust, normalized by $P_{ref}A^*$, is

$$\bar{\tau} = \bar{u}_e + \bar{p}_e a_e \qquad (35a)$$

where the second term contains no magnetic contribution because of our assumption that B=0 at and beyond the exit plane. The thruster efficiency is defined here as

$$\eta_{thr} = \frac{\text{Minimum power for a given thrust and flow}}{\text{Actual power}}$$

$$= \frac{1/2(\bar{F}/\bar{m})^2 - h_{to}}{\bar{V}\bar{I}}$$

or, in terms of the dimensionless variables,

$$= \frac{1/2\bar{F}^2 - \bar{h}_{to}}{\bar{J}\bar{V}} \qquad (35b)$$

The existence of an inlet discontinuity in the magnetic field distribution for a constant-area channel (and hence of an inlet current concentration) when $R\to\infty$ was already suggested in Ref. 4, but its magnitude was erroneously given as $1-b_1 = 1-2/3 = 1/3$. The error arose from the identification of $\bar{u}_1$ with $\bar{u}_0$. In the same paper, the inlet discontinuity was ignored when dealing with a convergent-divergent channel. We will see that this is justified only in the limit of very large inlet contraction ratio, although it may be a reasonable approximation for practical contraction ratios.

4.1 Sample Zero'th Order Results We have implemented the above procedures for both, a constant-γ gas model and an equilibrium Argon model allowing first ionization only, and verified these models against each other in low temperature cases. Two examples will be presented here, one for a convergent-divergent channel with $a_1=A_1/A^*=2$ and the other for a constant-area channel ($a = 1$). In both cases we assumed $\dot{m}/A^* = 0.5$ Kg/sec, B =0.1 Tesla , $T_{tot,o} = 400K$.

This means reference quantities u_{ref}= 7960 m/sec, P_{ref}= 3980 N/m , ρ_{ref}= 6.28×10^{-5} Kg/m^3, E_{ref}= 796 V/m, and also $h_{to} = 0.00328$.

Table 1 shows the principal results for the convergent-divergent channel. Several features of these results are noteworthy:

a) The flow is sub-magnetosonic (but mostly supersonic) in the "chamber" part of the channel.

b) There is a weak current concentration at inlet (carrying 1 - 0.9401, or 6%, of the total current).

c) Because of this last feature, the actual Argon temperature in the chamber is only 3100 K, too low for equilibrium ionization. Non-equilibrium effects should be accounted for, but this result emphasizes the "off-loading" of the channel inlet area.

d) There is a drastic density drop through even this weak current layer. This will hamper efforts at straight numerical simulation.

e) The ratio $\bar{p}$ of pressure to magnetic pressure remains at a few percent or below throughout the flow.

For comparison, Table 2 shows the results for a non-contoured, constant-area channel with otherwise the same data. The entire channel (except for the inlet and exit "layers") is now magnetosonic. The inlet region carries (1 - 0.63), or 37% of the current, the rest being carried by the exit current concentration. The extra inlet dissipation raises the Argon channel temperature to 7660 K (2.3% ionization, γ = 1.18) but it (and the exit concentration) lowers the efficiency, as shown in the exit nondimensional thrust of about 1.36 - 1 from MM effects, 0.16 from electrothermal expansion), compared to 1.61 for the case in Table 1. In fact, for the perfect expansion of Table 1, the thermal energy resulting from the inlet dissipation is fully recovered, and the thrust efficiency is unity; but even if we assume no recovery beyond the throat, an efficiency of 0.95 is calculated (ignoring, of course, all transport losses). By comparison, the

thrust efficiency of the constant-area channel is only 0.730. Note also the even more extreme density drop through the inlet layer in this case.

Notice that in both examples above the channel length is not specified, beyond stating that it must be large enough to make the Magnetic Reynolds number large. For $\sigma = 4000\,\Omega^{-1}/m$ we have (using Eq. (11)), $R_m = 40L$, with L in m. A 20 cm. long thruster would thus have $R_m = 8$, or $= 0.125$. We will see in Sec.5 that this value is *small enough to ensure a reasonably good* approximation from our zero'th order solution, including all the main qualitative features discussed.

4.2 Explicit Zero'th Order Results Neglecting Pressure . It was stated in Sec. 3 that gas pressure forces play a secondary role in MPD thrusters (except as discussed in Section 5.1, for low Rm, constant area cases) and this is to some extent verified by the low values of $\bar{p}$ in the results presented. It is therefore of interest to simplify the formulation by dropping $\bar{p}$ from the momentum equation (Eq. 14). This allows us to ignore the internal energy equation (Eq. 15), whose role is to determine p consistently, and also to drop any consideration of sonic passage, since the absence of any thermal effects essentially implies a very large inlet Mach number. We could now leave the inlet velocity $\bar{u}_o$ as an arbitrary parameter, or, provided we renounce calculation of $\bar{p}_o$, simply set it to zero. To illustrate the smallness of the effect of a finite $\bar{u}_o$, we will carry it as a parameter in the calculations.

Neglecting $\bar{p}$, Eq. (14) reads

$$\bar{u}\frac{d\bar{u}}{d\xi} + 2\frac{\bar{b}}{\bar{a}}\frac{d\bar{b}}{d\xi} = 0 \qquad (36)$$

and in the "outer" region, where $\frac{\bar{b}}{\bar{a}} = \bar{V}$, this integrates to

$$\bar{u}_0 = \sqrt{(u_1^0)^2 + 4\bar{V}(b_1^0 - b^0)} \qquad (37)$$

At the same time, $\bar{V} = \bar{u}^0 b^0 a$, so that the magnetic field b^0 in this outer region is related to the channel area through

$$a = \frac{\bar{V}}{\sqrt{b^{0\,2}\left[\bar{u}_1^{0\,2} + 4\bar{V}(b_1^0 - b^0)\right]}} \qquad (38)$$

Imposing that $a = 1$ when $da/db^0 = 0$ (throat) is equivalent to imposing magnetosonic choking. This gives the condition

$$(\bar{u}_1^{0\,2} + 4\bar{V}b_1^0)^{1/2} = 6\sqrt{3}\,\bar{V}^2; \quad \bar{u}_1^0 = \frac{\bar{V}}{a_0 b_1^0} \qquad (39)$$

In the "inner" region, equation (29) reduces now to

$$\bar{u}^1 = \bar{u}_0 + a_0(1 - b^{1\,2}) \qquad (40)$$

which, when substituted into the matching condition (32) gives

$$\frac{\bar{V}}{a_0} = b_1^0\left[\bar{u}_0 + a_0(1 - b_1^{0\,2})\right] \qquad (41)$$

Eliminating $\bar{V}$ between (31) and (41) gives an equation for b_1^0 as a function of a_0. The solution is best expressed inversely. Defining an intermediate variable x through

$$b_1^0 = \sqrt{\frac{1 + \bar{u}_0/a_0}{3}\,x} \qquad (42)$$

we find

$$a_0 = \sqrt{\frac{(x+1)^3}{4x^2(1-x)}} \qquad (43)$$

and then the voltage is

$$\bar{V} = \frac{(1+\bar{u}_0/a_0)^{1/2}}{4\sqrt{27}}\left(\frac{x+1}{\sqrt{x}}\right)^3 \qquad (44)$$

and the velocity at station (1) is given by

$$\bar{u}_1 = \left(1 + \frac{\bar{u}_0}{a_0}\right) a_0 \left(1 - \frac{x}{3}\right) \qquad (45)$$

Assigning values to x between 1 and 3 we thus obtain the results shown in Table 3, covering the range from no inlet contraction ($A_0 = A^*$) to infinite contraction ($A_0 \gg A^*$). For $a_0 = 1$ and $a_0 = 2$ these results can be compared to those in Tables 1 and 2, which include the pressure forces. For $a_0 = 1$, neglecting $\bar{p}$ gives $\bar{V} = 0.393$ if we take $\bar{u}_0 = 0.0147$ (Table 2), or $\bar{V} = 0.385$ with $\bar{u}_0 = 0$; the result in Table 1 is $\bar{V} = 0.458$. Better approximation is obtained for $a_0 = 2$ ($\bar{V} = 0.543$ using $\bar{u}_0 = 0.0143$, versus 0.566 from Table 1). It seems clear that neglecting thermal effects does give the correct trends, particularly when we compare other quantities as well.

To calculate the exit conditions we need to specify the exit area ratio $a_e = A_e/A^*$. The magnetic field just prior to the exit current concentration is not yet zero; denoting this location by the subscript (2) we can calculate b_2^0 by substituting $a = a_e$ into Eq. (38) and then $\bar{u}_2 = \bar{V}/a_e b_2$. Integrating the momentum equation, in the form of Eq. (36), across the exit "inner" layer then gives for the exit velocity ($b_e^0 = 0$):

$$\bar{u}_e = \bar{u}_2 + a_e(b_2^0)^2 \qquad (46)$$

It is noteworthy that this exit velocity can be explicitly written down as the product of two factors, one depending upon contraction ratio, $a_0 = A_0/A^*$, the other depending upon expansion ratio $a_e = A_e/A^*$. The result, after some algebra, is

$$\frac{\bar{u}_e}{1 + \bar{u}_0/a_0} = \varepsilon_0(a_0)\,\varepsilon_e(a_e) \qquad (47)$$

where

$$\varepsilon_0 = \left(\frac{x+1}{2\sqrt{x}}\right)^2 \quad (x \text{ given by Eq. 43}) \qquad (48)$$

$$\varepsilon_e = \frac{1 + 4\sin^2\phi}{4\sin\phi}; \quad \phi = \frac{1}{3}\left(\pi + 2\cos^{-1}\frac{1}{a_e}\right) \qquad (49)$$

The efficiency of the thruster reduces in this limit to

$$\eta = \frac{1/2\,\dot{m}\bar{u}_e^2}{\bar{V}I} = \frac{\bar{u}_e^2}{4\bar{V}} \qquad (50)$$

Combining Eqs. (47) and (44), this can also be expressed (in the present approximation) as the product of the factors

$$\eta = \eta_0(a_0)\eta_e(a_e) \qquad (51)$$

where

$$\eta_0 = \sqrt{\left(1 + \frac{\bar{u}_0}{a_0}\right)^3/4}\,\varepsilon_0 \qquad (52)$$

$$\eta_e = \left(\sqrt{3}\,\varepsilon_e\right)^2 \qquad (53)$$

The factors f_o and η_o are thus the exit velocity and efficiency of a purely convergent channel with a variable amount of pre-throat convergence, while f_e and η_e are the velocity and efficiency of a purely divergent channel of varying expansion area ratio. The limiting values (using $\bar{u}_o = 0$) are shown in Table 4.

Notice the strong beneficial effect of inlet convergence; divergence past the throat is also beneficial, but to a lesser extent. Even though no energy equation has been used, the implication of an efficiency less than unity is that some of the electrical energy IV, has been lost as thermal energy in the exhaust. The efficiency limit of 1 in the strongly convergent-divergent case is due to the elimination, in that limit, of the strong current concentrations both at inlet and at exit; it is these dissipative layers that are responsible for the inefficiencies in the other cases.

A word of caution is in order here. We have ignored the physical processes leading to ionization at the channel inlet. The amount of inlet contraction must be carefully balanced between the desire for high efficiency and the need for substantial ionization to ensure smooth plasma ignition.

5. Finite Magnetic Reynolds Number Effects

Beyond the zero'th order approximation in ε, analytical solution becomes much more difficult in the general case, although some additional results can be obtained for constant-area channels. Numerical methods must then be used to study the effects of finite magnetic diffusion. We will discuss separately the constant-area case, which is easier to analyze, but somewhat singular in its properties. Area variation effects will be then studied.

5.1 The Constant-Area Channel. From the work of Martinache [8] and King [9] it is well known that when $\alpha=1$ the quasi-one-dimensional conservation equations admit a full set of integrals by means of which all variables can be expressed as functions of the magnetic field, which can finally be related to distance through Ohm's law. In our notation, the first integrals are Eqs. (13) and (19), plus, from Eq. (24),

$$\bar{u} + \bar{p} + b^2 = \bar{u}_o + \bar{p}_o + 1 \tag{54}$$

The integration of Ohm's law (Eq. (16) and (17)) for the whole channel then gives

$$R_m = \frac{1}{\varepsilon} = \int_0^{\bar{R}} \frac{db}{\bar{E}-ub} \tag{55}$$

For a constant-γ gas model the conservation laws can be combined to yield a quadratic equation for $\bar{u}(b)$:

$$\frac{\gamma-1}{2\gamma}\bar{u}^2 - (1+\bar{u}_o+\bar{p}_o-b^2)\bar{u} + \frac{\gamma-1}{\gamma}[\bar{h}_{to}+\bar{E}(1-b)] = 0 \tag{56}$$

The two branches of the solution to (56) are the subsonic and supersonic velocities for a given b. Smooth sonic passage can be assured by forcing the discriminant of Eq. (56) to have a minimum value of zero at some $b = b_s$. This gives two equations relating the parameters b_s and $\bar{u}_o+\bar{p}_o$ to the field $\bar{E}$. Therefore, one can pick a value of $\bar{E}$, calculate $\bar{u}_o+\bar{p}_o$, solve (56) for u for each b, and calculate $\varepsilon(\bar{E})$ by performing the integration in (55).

The least $\bar{E}$ possible clearly corresponds to the maximum of the quantity $\bar{u}\,b$, since otherwise Eq. (55) is singular. For $\bar{E}$ just slightly above this maximum, the magnetic Reynolds number $R_m = 1/\varepsilon$ is very large, and its value decreases as $\bar{E}$ is increased. An example for $\bar{E}$ very near $\bar{E}_{min}$ is shown in Fig. 1, where one can see the strong inlet and exit current concentration and flow acceleration regions, the small level of $\bar{p}$ and the predominance of the back e.m.f. $\bar{u}\,b$ over the ohmic fall $\bar{E}-\bar{u}\,b$ over the body of the channel. Notice also that, despite the smallness of $\bar{p}$, its gradient is strongly positive near the exit, due to the ohmic heating in that region with negligible magnetic acceleration (small $-\bar{b}d\bar{b}/d\bar{x}$). This pressure gradient is seen to decelerate the flow near the exit. This feature becomes more severe as the magnetic Reynolds number is reduced, eventually leading to thermal choking, and is a peculiarity of the constant-area geometry, aggravated by the somewhat artificial $b_e = 0$ condition.

For an R_m of about 5, Fig. 2 shows substantial deceleration near the exit, with the Mach number (dotted line) approaching unity. Further reduction to $R_m = 3.4$ (Fig. 3) leads to exit thermal choking, which forces a mid-channel shock (mathematically, a transition from the upper to the lower branch of Eq. (56)) and a subsonic downstream section ending at M=1. In this section the pressure $\bar{p}$ is no longer small. It is noteworthy that positioning the shock further upstream leads to a lower R_m, but, if $\bar{h}_{to}$ is held constant, there is no change in $\bar{E}$ or the exit conditions, as long as the flow has a supersonic section. A more realizable condition would be a constant $\bar{h}_{to}$ (dimensional), which can be seen to imply $h_{to} \propto R_m$ = const., but numerical calculations show only a secondary effect of $\bar{h}_{to}$ over the range of physical interest.

Eventually, as R_m decreases, the shock reaches the sonic transition point, and the whole channel becomes subsonic. Beyond this condition, further reductions of R_m do increase $\bar{E}$ (mathematically, once the freedom offered by shock location is lost, R_m can be reduced in Eq. (55) only by increases of $\bar{E}$). Since by now $u\,b \ll \bar{E}$ (mostly Ohmic voltage), the extreme (electrothermal) limit of Eq. (55) is

$$R_m = \frac{1}{\varepsilon} \sim \bar{E} \tag{57}$$

The terminal characteristics of a series of channels with constant inlet enthalpy (roughly corresponding to 4000K Argon) are shown in Fig. 4. The leveling of $\bar{E}$, η_{th} and $\bar{F}$ in the mixed-flow regime is clearly visible, as is the eventual Ohmic electrical behavior ($\bar{E} \sim 1/R_m$ implies $V \sim I$) and electrothermal thrust variation ($\bar{F} \sim 1/R_m$ implies $\bar{F} \sim \dot{m}$). Notice that for this simple geometry $\bar{E} = 1$ would be the pure electromagnetic result, so that the excess seen in $\bar{E}$ at low R_m is the electrothermal contribution (which, as noted in Sections 4.1, 4.2, is non-zero even at $R_m \to \infty$). Notice, finally the quadratic behavior of $\bar{E}(\varepsilon)$ as $\varepsilon \to 0$; this can be analytically proven by expanding $\bar{E}-ub$ about its minimum value, which contributes

the most to Eq. (55). The $Rm \to \infty$ approximation is seen to provide ~10% accuracy for $Rm \geq 10$. Once again, much of the inaccuracy is traceable to the strong localized heating peculiar to the constant-area geometry, as will become more clear in the following.

5.2 Convergent-Divergent Channel For $a = a(\xi)$ the momentum equation does not integrate immediately, and the set of equations (13)-(18) must be integrated numerically in $0 \leq \xi \leq 1$. For this purpose, the derivatives must be explicitly solved for, as was done in Eq. (33) for $\frac{d\bar{u}}{d\xi}$. In terms of $\frac{d\bar{u}}{d\xi}$,

$$\frac{d\bar{p}}{d\xi} = -\frac{1}{a}\frac{d\bar{u}}{d\xi} + \frac{2b}{\varepsilon}(\bar{E}-\bar{u}b) \qquad (58)$$

and, of course,

$$\frac{db}{d\xi} = -\frac{1}{\varepsilon}(\bar{E}-\bar{u}b) \qquad (59)$$

Alternatively, equation (58) can be replaced by algebraic solution of the total energy equation (Eq. (19)) for $\bar{p} = \bar{p}(\bar{u}, b)$.

The only known initial condition (at $\xi=0$) is $b(0)=1$. The initial velocity $\bar{u}(0)$ must be guessed, and then $\bar{p}(0)$ can be calculated from $p=a=1$ and the given h_{t_0}. We also need to guess the parameter $\bar{E} = \bar{V}/\bar{A}^0$. The correct values of $\bar{u}_0$ and $\bar{E}_0$ must satisfy (iteratively) the two downstream conditions

(a) Smooth passage through the ordinary speed of sound
(b) $b(1) = 0$

Notice that the last condition replaces the condition of magnetosonic throat choking which was used in the 0th order solution. In fact, it is only for $\varepsilon \to 0$ that strict magnetosonic choking occurs, just as it is only for purely inviscid flow that an ordinary nozzle flow becomes sonic at a throat. In the presence of finite magnetic diffusion effects (finite Rm), the effect of the downstream condition $b(1)=0$ can be felt, although weakly, throughout the channel.

Forward integration of these equations is made difficult by the existence of the critical sonic point and the near-critical magnetosonic point. The procedure followed was to select values of $\bar{u}_0$ and $\bar{E}_0$ and integrate using the 4th order Runge-Kutta method to the sonic point, where rapid divergence was usually encountered. The value of $\bar{E}_0$ was then modified and the calculation re-started, until a sufficiently smooth sonic passage was achieved. Once this happened, a second divergence was typically encountered near, but somewhat beyond the throat, this forced repetition of the whole process with a new $\bar{u}_0$, until eventually the $b(1)=0$ condition was met.

For illustration, a convergent-divergent area distribution was generated with $a_0=2$, such as to obtain a linear pressure profile between Mach numbers of $M=0.297$ and $M=5$ in cold Argon flow. This same area was then used for MPD calculations with $\varepsilon = 0$, 0.1 and 0.3, using an ideal gas model with $\gamma = 5/3$ and $h_{t_0} = 0.00328$. The results for $\varepsilon = 0.3$ ($Rm=3.333$) are shown in Fig. 5, where several features can be noticed:

(a) No current concentration is seen near the inlet or exit, and the current density is about uniform in the channel.

(b) There is no positive pressure gradient (in fact there is a negative one) near the exit, so the flow is never decelerated.

(c) The Mach-Alfven number (MA) is slightly less than unity at the throat, and crosses to MA>1 in the divergent part of the nozzle.

These features generally confirm the analysis made for $Rm \to \infty$, despite the fairly low Rm chosen. In contrast, the constant-area channel of Fig. 3, for a comparable Rm, showed strong electrothermal features. This difference clearly illustrates the potential of area contouring for improving MPD thruster efficiency and, by reducing current concentrations, extend electrode life.

Fig. 6 shows how the inlet field $\bar{E}(0)$, inlet density $\bar{\rho}(0)$ and Mach-Alfven number at the throat (MA thr.) evolve as the magnetic Reynolds number decreases from infinity to about 3. Clearly, the salient features of the $Rm=\infty$ limit are recognizable down to $Rm \simeq 3$, with only a slight increase of $\bar{E}$ throughout this range (this, of course, implies a nearly cubic V(I) characteristic). The throat speed is confirmed to be quite close to magnetosonic in this range of Rm. The large values of $\bar{\rho}(0)$ reflect the smallness of $\bar{u}(0)$; since u increases rapidly away from $\xi=0$, there is in all cases a very rapid density decline, which will be very difficult to resolve by numerical grids in multidimensional computations.

6. Comparison to Experimental Data. A recent paper by R.G. Jahn and A.J. Kelly provides a set of thrust and voltage data from a small MPD thruster with an area distribution which is flared at first, and then continues for the greater part of its length with constant cross-section. These data are doubly useful in that they are presented in non-dimensional terms, using parameters which are, however, different from ours. The parameters are chosen to emphasize the importance of the Alfven critical ionization phenomenon. Thus, the choice reference voltage is

$$V_{ref} = (2\, b_{th}\, V_{ac}^3)^{1/2} \qquad (60)$$

$$b = \frac{\mu_0 I}{4\pi} \ln \frac{r_a}{r_c} \quad ; \quad V_{ac} = \left(\frac{2\epsilon_i}{m_i}\right)^{1/2} \qquad (61)$$

where r_a and r_c are the anode and cathode radii, ϵ_i is the ionization energy, and m_i the ion mass and V_{ac} is the Alfven critical velocity. The reference current is

$$I_{ref} = \left(\frac{\dot{m}\, V_{ac}}{\mu_0}\right)^{1/2} \qquad (62)$$

We have converted the results of Fig. 4 of this paper (constant area, $\gamma=5/3$) to these new parameters, and superimposed them on the curve of dimensionless voltage vs. dimensionless current of Ref. 9. This is shown in Fig. 7, which also contains the predictions of the Alfven critical speed model. It can be seen that the fit is very good at high current (the un-choked range), but the theory under-predicts the linear part of the voltage (the subsonic range). This is possibly

due to our neglect of any finite ionization effects in the results of Fig. 4. These calculations should be repeated using a more realistic (equilibrium ionization) gas model. The important point, however, is that the linear-to-cubic transition appears naturally with no need to invoke critical ionization events, and is therefore seen to be a reflection of the basic gas-dynamics of the device.

We have also compared the thrust vs. current predictions of Fig. 4 to the data reported in Ref. 9. These data are normalized to emphasize the quadratic dependence on current at high $I^2/\dot{m}$ values. The results are shown in Fig. 8. The theory overpredicts thrust in the electromagnetic-dominated range (probably due to some misrepresentation of the geometrical effects plus the neglect of friction, but it reproduces very well the transition to the electrothermal-dominated range.

7. Conclusions and Discussion Despite our limitation to quasi one-dimensional flows, several important features of self-field accelerated flows have been identified:

. For reasonably large Magnetic Reynolds numbers, geometrical throats are nearly magnetosonically choked.

. Under the same conditions, the channel transverse voltage is dominated by the local back emf, except near inlet and exit.

. These two properties together essentially determine the voltage for a given current and flow rate.

. Ordinary sonic passage occurs well upstream of the throat, and its role is mainly to determine conditions at the injector plate,

. Except for constant area channels, where the strong inlet and outlet current concentrations produce important thermal effects, the role of ordinary pressure forces in determining flow and terminal properties is quite limited.

. Approximate factors can be derived to separately quantify the performance gains due to inlet convergence and nozzle divergence.

. Comparison to experimental data on terminal characteristics confirms several of the trends shown by this theory. In particular, the electrothermal-electromagnetic transition is well predicted, with no need to invoke ablation or critical ionization effects.

Many of these properties are likely to be of use in multidimensional modeling of MPD flows. For instance, approximate flow fields can be computed much more easily by neglecting axial pressure forces while retaining them in the transverse directions to balance pinching magnetic forces; difficulties associated with transonic flow are thus obviated. It is also useful to recognize the dominance of the back emf over ohmic fields, provided current concentration layers are treated separately. Finally, such current concentrations can be minimized by the same sort of careful aerodynamic shaping as exercised by ordinary nozzle designers.

To conclude, it must be recalled that throughout this analysis we have assumed no net axial current, and hence no gross transverse nonuniformity. While this is a realizable condition, many experimental accelerators are in fact strongly affected by axial current and pinching magnetic forces, so that our results have only a qualitative validity in such cases; in particular, the dramatic electrical effects of anode depletion ("onset") are not predictable by this type of theory.

References

1. D. King, K.E. Clark and R.G. Jahn, "The Effect of Choked Flow on Terminal Characteristics of MPD Thrusters", 15th Intnl. Electric Propulsion Conference, Las Vegas, Nevada, 1981.

2. J.L. Lawless and V.V. Subramanian, "Theory of Onset in Magnetoplasmadynamic Thrusters", J. Propulsion, Vol. 3 No. 2, pp. 121-127 March-April, 1987.

3. M. Martinez-Sanchez and D. Heimerdinger, "Two-dimensional Analysis of an MPD Arcjet", AIAA Paper 85-2040, Intnl. Electric Propulsion Conference, Alexandria, VA, 1985.

4. F.G. Baksht, B.Y. Moizhes and A.B. Rybakov, "Critical Regime of a Plasma Accelerator", Sov. Phys. Tech. Phys., Vol. 18, No. 12, June 1974.

5. L.K. Rudolph, R.G. Jahn, K.E. Clark and W.F. Von Jaskowsky, "Onset Phenomena in Self-Field MPD Arcjets", AIAA Paper 78-663, 13th Intnl. Electric Propulsion Conference, San Diego, CA, 1978.

6. J. Barnett "Operation of the MPD Thruster with Stepped Current Input", Ph.D. Dissertation, Princeton University, Princeton, NJ, 1985.

7. K. Kuriki and M. Onishi, "Thrust Measurement of KIII MPD Arcjet", AIAA Paper 81-0683, 15th Intnl. Electric Propulsion Conference, Las Vegas, Nevada, 1981.

8. G.M. Martinache "A Theory of a Parallel Plate Accelerator", Ph.D. Dissertation, Princeton University, Princeton, NJ, 1987.

9. R.G. Jahn and A.J. Kelly "Megawatt Level Electric Propulsion Perspectives", Presented at the Open Sessions of the 4th Symposium on Space Nuclear Power Systems, Albuquerque, New Mexico, Jan. 1987.

Location	b	a	$\bar{u}$	$\bar{\rho}$	$\bar{E}$	Mach #	Mach # (Vibration)
Inlet	1	0.0143	34.9892	0.9449	0.2832	0.0114	0.5[illegible]
Sonic Point	0.9793	0.1157	4.3229	0.3147	0.2832	1	0.[illegible]
Edge of Inlet Lever	0.9401	0.3012	1.8899	0.0171	0.2832	2.2987	0.2898
Throat	0.8929	0.4899	1.1524	0.3093	0.5464	1.4774	1
Exit (Infinite Expansion)	0	1.5073	0	0	0	∞	∞

TABLE 1. NONDIMENSIONAL QUANTITIES FOR CONVERGING-DIVERGING CHANNEL

Location	b	a	$\bar{u}$	$\bar{\rho}$	$\bar{E}$	Mach #	Mach # (Vibration)
Inlet	1	0.0147	115.00	0.1520	0.4576	0.187	0.5637
Sonic Point	0.9304	0.1786	5.598	0.1156	0.4576	1	0.3058
Channel	0.4276	0.9260	1.3717	0.0360	0.4576	4.186	1
Exit Plane ($\bar{\rho} = .01$)	0	1.1212	0.8919	0.0374	0.4576	5.238	5.238

TABLE 2. NONDIMENSIONAL QUANTITIES FOR CONSTANT AREA CHANNEL

Table 3 - Solutions Neglecting Pressure Forces

x	1	1.25	1.5	1.75	2	2.25	2.5	2.5693	2.75	2.875	3
a_o	1	1.0205	1.07583	1.1436	1.29906	1.50343	1.85201	2	2.44067	3.25219	∞
$\frac{b^o}{(1+\bar{u}_o^2/a_o^2)^{1/2}}$	$1/\sqrt{2}$ 0.70735	0.64550	0.70711	0.76376	0.81650	0.86603	0.91287	0.92547	0.95743	0.97895	1
$\frac{u^o}{(1+\bar{u}_o^2/a_o^2)}$	2/3	0.59529	0.53791	0.48558	0.43301	0.37586	0.32867	0.28101	0.22006	0.13634	0
$\frac{\bar{v}^o}{(1+\bar{u}_o^2/a_o^2)^{3/2}}$	$2/\sqrt{27}$ 0.38490	0.39214	0.40921	0.43221	0.45929	0.48938	0.52186	0.53126	0.55638	0.57627	0.59256

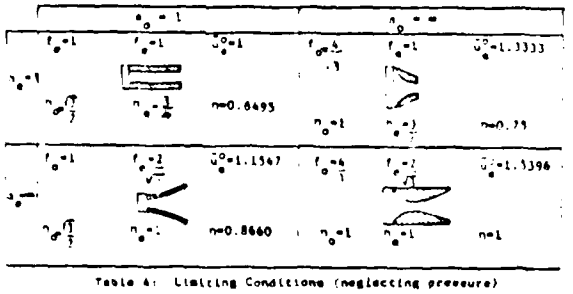

Table 4: Limiting Conditions (neglecting pressure)

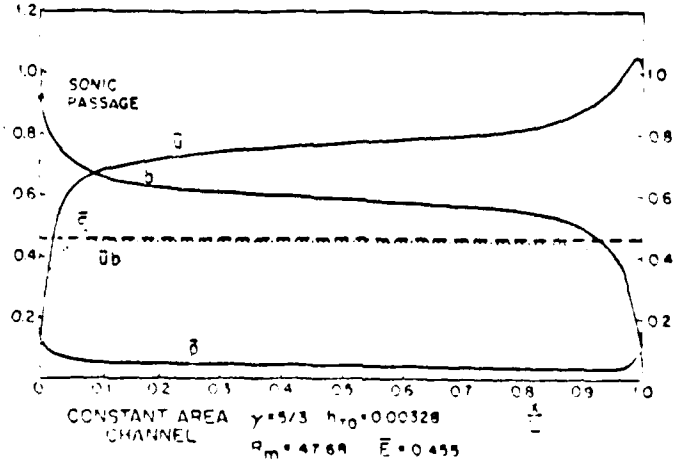

Figure 1

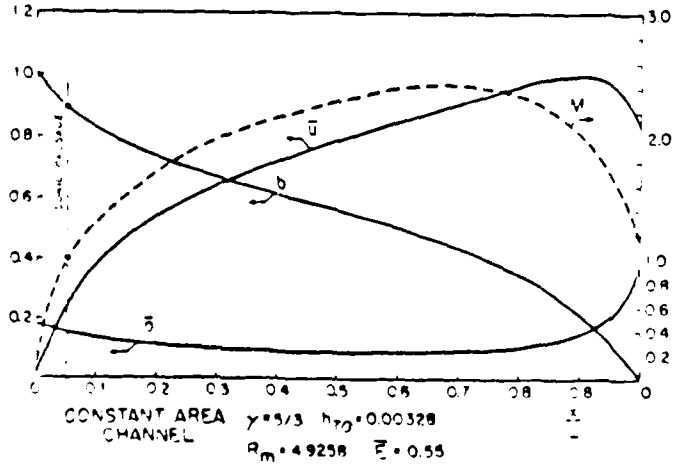

Figure 2

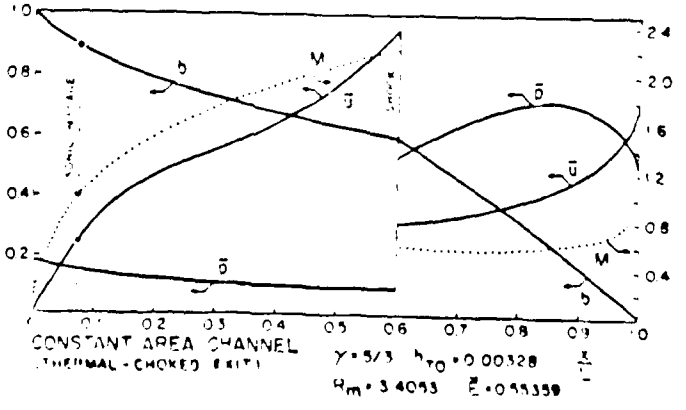

Figure 3

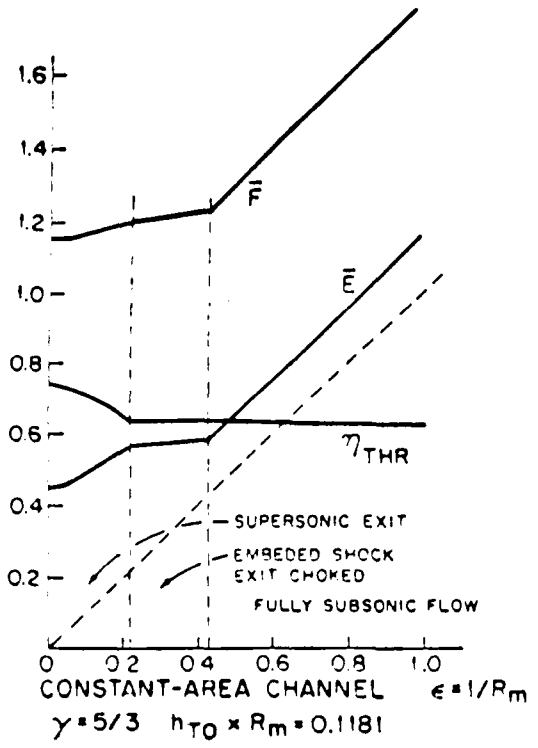

Figure 4: Terminal characteristics of constant area channels with $\gamma = 5/3$ and $T_{tot_o} = 400$ K (Argon).

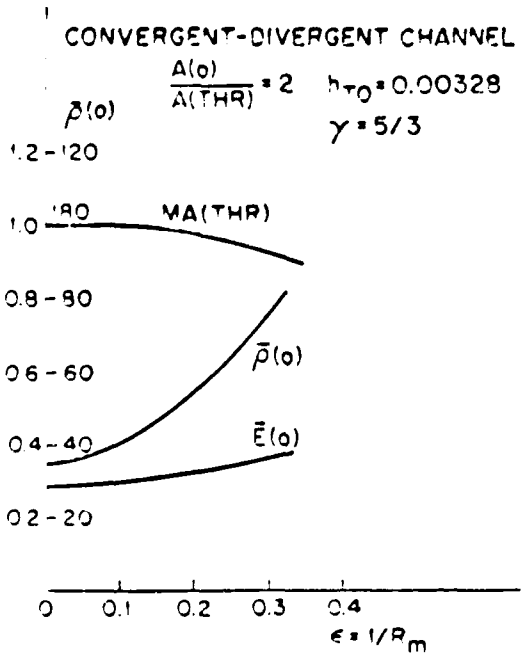

Figure 6: Characteristics of convergent-divergent channels; Mach/Alfven No. at the throat, density at injector plate and transverse field versus Magnetic Reynolds No.

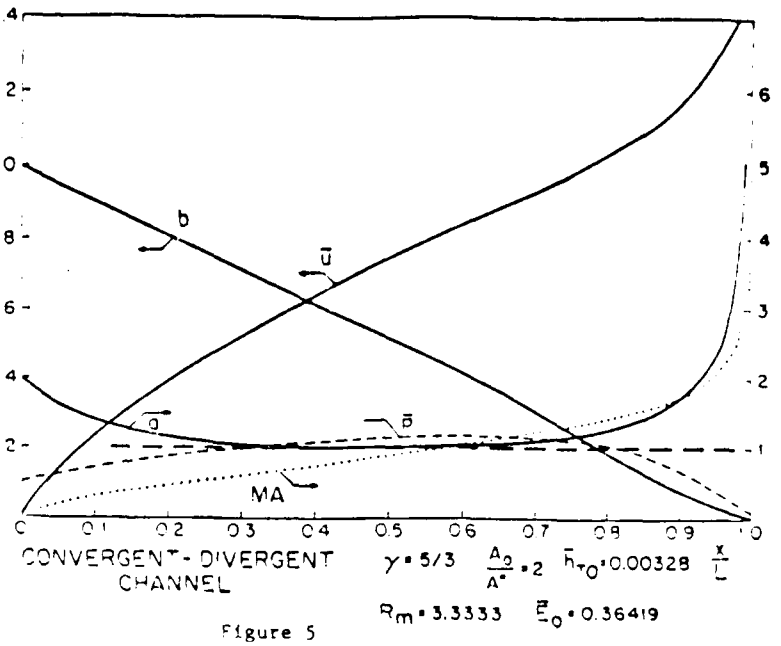

Figure 5

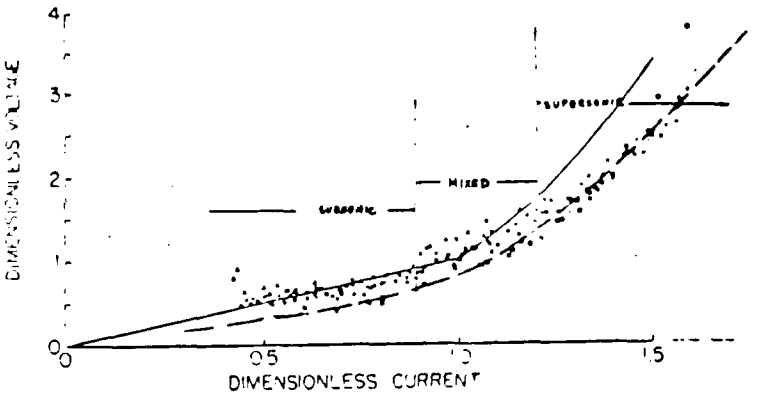

Figure 7: Voltage-Current Characteristics Data from Ref. 9. Solid line: theory from Ref. 9. Broken line: this work, with: $\sigma = 30000 \Omega^{-1}/m$, L=9cm, H/W=.21, argon gas.

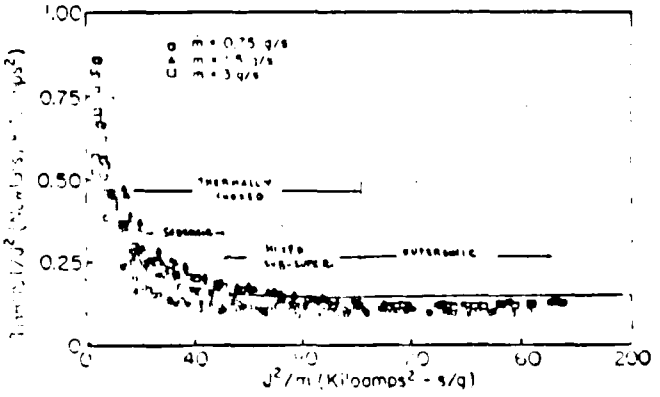

Figure 8: Thrust vs Current Data from Ref. 9. Line from this work, assuming constant area, $\sigma = 30000 \Omega^{-1}/m$, L=9cm, H/W=.21, argon gas.

APPENDIX II

AIAA-87-1090
Two-Dimensional Numerical Simulation of MPD Flows

J. M. G. Charty and M. Martinez-Sanchez,
Massachusetts Institute of Technology,
Cambridge, MA

AIAA/DGLR/JSASS 19th International
Electric Propulsion Conference
May 11-13, 1987
Colorado Springs, Colorado

AIAA-87-1090

Two-Dimensional Numerical Simulation of MPD Flows

J. M. G. Chanty*, M. Martinez-Sanchez†

Space Systems Laboratory, Department of Aeronautics and Astronautics

Massachusets Institute of Technology, Cambridge, MA. 02139

Abstract

A two-dimensional numerical model has been developed in order to analyse electro-magnetic plasma accelerators also called Self-Field Magneto-Plasma-Dynamic Thrusters. This model uses a Magneto-Hydro-Dynamic description of the gas considered as a fully ionized, isothermal plasma, and takes into account the Hall effect (non linear conductivity) and the interaction between the magnetic field and the fluid dynamics of the plasma. The system of equations is discretised into finite volumes, and is solved by a Newton-Raphson scheme. Results from the MHD model were calculated for a mass flow rate of 6 g/s of Argon and for currents up to ten kilo-Amperes.

Introduction

During the past years the development of high current plasma accelerators (also called Magneto-Plasma-Dynamic Thrusters) has been aimed, among other things, at improving the efficiency of energy conversion from electrical to kinetic energy. Several researchers have observed that the efficiency increases with the current, but at some value a transition occurs to an unstable and destructive regime of the discharge (called onset of instability in the literature), when the ratio $\frac{I^2}{\dot{m}}$ exceeds a critical value which depends on the nature of the propellant and the thruster geometry. Some researchers [3] [11] have proposed a theory for the transition to an unstable behavior based on the depletion of the anode from current-carrying electrons, the formation of a starvation layer along the anode characterized by current densities in excess of the random thermal flux of electrons, and the reversing of the potential drop between the the plasma and the electrode. In order to study the formation of this starvation layer one needs to take the geometrical properties of the discharge into account, or in other words, to look at a two-dimensional model of the discharge. Eventually this model can be used to find optimal shapes that maximise certain parameters like efficiency or electrode life.

Various attempts have been made to develop numerical two-dimensional models of MPD discharges using finite element or finite difference descriptions. I. Kimura et al. [17] have presented a two dimensional model for the electromagnetic field (self field), including the Hall effect. The model was primarily designed to calculate the current distribution near the cathode. They later extended their model [27] to systems that work with an external focussing magnetic field. These models, however, were not designed for an accurate modelling of realistic thruster geometries, and did not include the effect of the convection of the electromagnetic field by the plasma. This last limitation was partially removed in a later paper [28] where a simplified calculation of the flow was made and coupled with the magnetic field. Ao and Fujiwara [1] have attempted to develop a one-fluid Magneto-Hydro-Dynamic model of the plasma where the equations describing the motion of the plasma, considered as a neutral conductive fluid, are coupled with the magnetic field through the Lorentz force and the ohmic heating. However this model was limited to a very simple geometry.

It was decided to develop a two-dimensional numerical model based on a MHD description of the plasma in the collision dominated regime, in order to calculate the steady state distribution of the electro-magnetic field and the motion of the plasma in the accelerator. We focused our attention on the phenomena observed at the electrodes, especially at the anode, in an effort to detect the onset of the turbulent regime.

The system of partial differential equations is discretised using a finite volume technique used extensively in Computational Fluid Dynamic algorithms. The system of equations was solved using a Newton-Raphson method, derived from an initial calculation of the magnetic field alone for which this method works well due to the dominant elliptic behavior of the equations. The method of discretisation of the equations (finite volume method) as well as the idea of the addition of an artificial viscosity, was derived from Jameson and Yoon [15]. A confirmation of the possibility of the Newton-Raphson method was found in the lecture of Jespersen [16], as well as in the doctoral theses of M. Giles [8] and M. Orela [7].

*Graduate Student

†Associate Professor

Physical Model

The equations describing the model are derived from the general Magneto-Hydro-Dynamic approximation which includes the following equations: conservation of mass, momentum and energy in the inviscid fluid; the Ohm's law (derived from the electron momentum conservation); and the quasi-static Maxwell's equations.

$$\partial_t \rho + \nabla(\rho \mathbf{u}) = 0$$

$$\partial_t \rho \mathbf{u} + \mathrm{Div}(\rho \overline{\overline{\mathbf{uu}}} - \overline{\overline{S}} - \overline{\overline{M}}) = 0$$

Where $\overline{\overline{S}}$ is the pressure stress tensor, and $\overline{\overline{M}}$ is the Maxwell stress tensor.

$$\partial_t (E_{EM} + E_I + E_K) + \nabla \cdot ((E_I + E_K + P)\mathbf{u} + \frac{\mathbf{E} \times \mathbf{B}}{\mu_0} + \mathbf{q}) = 0$$

Where E_{EM}, E_I, E_K are respectively the electromagnetic energy ($B^2/2\mu_0$), the internal energy, and the kinetic energy, per unit volume; P is the pressure; $\frac{\mathbf{E} \times \mathbf{B}}{\mu_0}$ is the Poynting vector; $\mathbf{q}$ is the heat conduction. The energy-equation is usually completed by a state equation relating the pressure to the internal energy, for instance :

$$P = (\gamma - 1) E_I$$

The generalised Ohm's law can be written as:

$$\mathbf{E} + \mathbf{u} \times \mathbf{B} = \frac{1}{\sigma}\mathbf{J} + \frac{1}{e n_e}\mathbf{J} \times \mathbf{B} - \frac{\nabla P_e}{e n_e}$$

The Maxwell's equations reduce to:

$$\nabla \times \mathbf{E} = -\partial_t \mathbf{B} \qquad \nabla \mathbf{B} = 0$$

$$\nabla \times \mathbf{B} = \mu_0 \mathbf{J}$$

We have assumed that the field is quasi-static and that the plasma is approximately neutral.

Let us now look at the possible simplifications:

Geometry: The flow and the electromagnetic field are axisymetric. There is no externally imposed magnetic field. The Magnetic field is therefore azimuthal.

The Ohm's Law and the electromagnetic equations are combined in order to eliminate $\mathbf{E}$ and $\mathbf{J}$. One obtains an equation in $\mathbf{B}$ that describes the diffusion and convection of the magnetic field in a conducting medium:

$$\nabla \times (-\mathbf{u} \times \mathbf{B} + \frac{\nabla \times \mathbf{B}}{\mu_0 \sigma} + \frac{(\nabla \times \mathbf{B}) \times \mathbf{B}}{\mu_0 e n_e} - \frac{\nabla P_e}{e n_e}) = -\partial_t \mathbf{B}$$

Rewriting the equation in non-dimensional form,

$$-\partial_{t^*} \mathbf{B}^* + \nabla^* \times (\mathbf{u}^* \times \mathbf{B}^*) =$$

$$\frac{1}{R_m} \nabla^* \times (\frac{\nabla^* \times \mathbf{B}^*}{\sigma^*} + H_e (\frac{(\nabla^* \times \mathbf{B}^*) \times \mathbf{B}^*}{n_e^*} - \frac{\beta}{2} \frac{\nabla^* (n_e^* T_e^*)}{n_e^*}))$$

introduces three non-dimensional numbers: $N_1 = \frac{1}{R_m}$ for the magnetic diffusion due to conductivity; $N_2 = \frac{H_e}{R_m}$ for the non linear Hall effect; $N_3 = \frac{\beta H_e}{2 R_m}$ for the electron diffusion. $R_m = \mu_0 \sigma_0 u_0 L_0$ is the magnetic Reynolds number, based on the distance between the electrodes; H_e is the Hall parameter;

$$H_e = \frac{B_0 \sigma_0}{e n_{e0}} = \omega_{ce} \tau$$

where ω_{ce} is the electron cyclotron angular frequency and $\tau_e = 1/\nu_e$ is the electron collision time . β is the plasma-β; ratio of the pressure to the magnetic pressure,

$$\beta = \frac{2\mu_0 P_e}{B_0^2}$$

The values of these non-dimensional numbers give an indication of the relative importance of each phenomenon: Inside the channel $N_1 \approx 0.5$, $N_2 \approx 0.6$, $N_3 \approx 0.03$. Therefore we take the Hall effect and the convection into account, but we neglect the effect of the electron pressure gradient on the conductivity. (Notice that a magnetic Reynolds Number based on the channel length would be of order 5 to 10).

Constant temperature approximation: In a plasma like the one considered here, the energy equation is the most difficult to justify. At high temperature (around 12500 K) the gas is strongly ionised and radiates energy. These processes are not necessarily in equilibrium and therefore cannot be accurately described by the energy conservation equation used in the fluid theory at low temperatures. As in most MHD models the energy conservation equation will be dropped and replaced with the assumption that the plasma is roughly isothermal. This assumption can be justified by the effect of ionisation which tends to oppose any change in temperature by a displacement of the ionization equilibrium, by the thermal conductivity of the plasma, and by the value of the pressure relative to the magnetic pressure $\beta \ll 1$. The non-dimensional number describing the balance between kinetic energy and heat conduction (equivalent of the Reynolds number for the energy equation) is:

$$C_l = \frac{L_0 \rho_0 U_0^3}{\kappa T_0}$$

Its value goes from ≈ 200 in the cathode jet, to ≈ 1 along the external surface of the anode.

Conductivity: In the Spitzer-Härm aproximation the conductivity of a fully ionized plasma is proportional to $T^{\frac{3}{2}}$. Consequently we have a constant value for the electrical conductivity $\sigma = 3000\,\mathrm{Si/m}$.

Even though the energy balance is not written, the fact that one part of the electrical work $\mathbf{E} \cdot \mathbf{J}$ is dissipated ohmically as $\frac{J^2}{\sigma}$ is implicit in the rest of the formulation, and therefore a meaningful thruster efficiency can be computed. What is ignored is the ultimate fate of the ohmic heat and its apportionment to ionisation, heat conduction, radiation, etc.

Since ionisation processes are not covered in the model, the plasma is considered fully ionised when it enters the inlet of the accelerator.

Although the real Reynolds number is of the order of 100 to 200, the plasma is considered inviscid, which means that second order derivatives appear only in the electromagnetic equation.

The final set of equations after simplifications is then:

$$\partial_z(\rho u_z) + \frac{1}{r}\partial_r(r\rho u_r) = 0$$

$$\partial_z(\rho u_z u_z + P + \frac{B^2}{2\mu_0}) + \frac{1}{r}\partial_r(r\rho u_z u_r) = 0$$

$$\partial_z(\rho u_z u_r) + \frac{1}{r}\partial_r(r(\rho u_r u_r + P + \frac{B^2}{2\mu_0})) + \frac{-P + \frac{B^2}{2\mu_0}}{r} = 0$$

$$P = \rho R T_0$$

$$\oint \mathbf{E}\mathrm{d}\mathbf{l} = 0$$

$$E_z = \frac{1}{\mu_0\sigma}\frac{1}{r}\partial_r rB - \frac{B}{\mu_0 e n_e}\partial_z B - u_r B$$

$$E_r = -\frac{1}{\mu_0\sigma}\partial_z B - \frac{B}{\mu_0 e n_e}\frac{1}{r}\partial_r rB + u_z B$$

The boundary conditions were taken as follows:

The tangential electric field is zero on the electrodes. The electrodes include the conducting surfaces of the anode and the cathode. The voltage drop across the plasma-sheath, which extends over a few Debye lengths inside the plasma, will be neglected. Consequentely the voltage drop across the channel will be underestimated when the anode is starved, i.e. at high current densities.

The entrance surface (the back plate) is an insulating surface which carries the injector holes. It is assumed that the gas is injected uniformly across the back plate, which would be the case with a porous back plate or with a plate containing a large number of injector holes. A transition between the gas state, characterised by a low temperature and a low conductivity, and the plasma state, where the gas is ionised and is a good conductor of electricity, arises once the gas is in the annular chamber. This ionisation takes place in a region close to the back plate surface. The calculation starts after the ionisation layer assuming that the gas has reached a uniform temperature of 12500 K, at which the electrical conduction is sufficently high to consider the gas as a plasma. Across the entrance plane the magnetic field is: $B = \mu_0 I/2\pi r$. The dynamic variables $\rho, \rho u_z, \rho u_r$ are specified along the entrance surface : $\rho u_r = 0$; ρu_z is specified by the mass flow rate:

$$\rho u_z = \frac{\dot{m}}{A_{inlet}}$$

The existence of a steep density gradient immediately adjacent to the back plate makes it very difficult to resolve this layer numerically. Fortunately one of us has shown [22] that the details of the inlet gradients have only a small influence downstream. In our calculation we assign an arbitrary value to ρ.

On the outer boundary of the computational domain (i.e. far into the plume) $B = 0$. This condition means that there is no current going outside the boundary of the calculation, which is therefore an insulating surface. There are no gradients of ρ, ρu_z, ρu_r along the direction parallel to the flow.

On the axis of symetry $B = 0$.

Numerical Method

The system of equations is solved by the Newton-Raphston method using the technique of Finite Volumes for the discretisation of the equations of motion, and a technique similar to the method of finite volumes for the magnetic field. Artificial viscosity is added to the equations of motion in order to avoid non-linear instabilities at places of strong density gradients. The conservation equations are discretised according to the method of finite volumes: The computational space is divided into 20 × 41 quadrilaterals. The grid is shown in figure 1. The variables $(\rho, \rho u_z, \rho u_r, B)$ are approximated by their space-average on each quadrilateral. The equations are written in their integral form:

$$\oint_S \rho u \mathrm{d}^2\mathcal{S} = 0$$

$$\oint_S (\rho\overline{\overline{uu}} - \overline{\overline{S}} - \overline{\overline{M}})\mathrm{d}^2\mathcal{S} = 0$$

where the the tensor $\rho\overline{\overline{uu}} - \overline{\overline{S}} - \overline{\overline{M}}$ has the following physical components in cylindrical coordinates (z, r, ϕ) :

$$\begin{bmatrix} \rho u_z u_z + P + \frac{B^2}{2\mu_0} & \rho u_z u_r & 0 \\ \rho u_z u_r & \rho u_r u_r + P + \frac{B^2}{2\mu_0} & 0 \\ 0 & 0 & P - \frac{B^2}{2\mu_0} \end{bmatrix}$$

Since the problem is axisymetrical, the volume elements are obtained by rotating the quadrilaterals that define the grid cells by an infinitesimal angle $\Delta\phi$ around the axis of symetry. The surface integral around each element is broken into six integrals, one for each facet. Each of them is discretised by assuming that the fluxes are constant on each facet of the boundary. For the electro-magnetic field one uses a different integral (line integral over a closed contour):

$$\oint_C \mathbf{E}\mathrm{d}\mathbf{l} = 0$$

The contours are defined by the same quadrilaterals as above. For each iteration the Newton-Raphson algorithm

inverts a matrix of order 3200 which represents the system of partial differential equations linearized at the current estimate of the solution vector. This takes about 10 minutes on a microVax. One needs about 10 iterations to attain convergence.

Experimental Background

Experimental studies have identified three modes of operation for the plasma accelerator: electrothermal mode, for which the dominant acceleration mechanism is the expansion of the heated gas across the thermodynamic pressure gradient; electromagnetic mode, for which the dominant acceleration mechanism is the expansion of the gas across the magnetic pressure gradient; finally the unstable regime which set on when the critical ratio $\frac{I^2}{\dot{m}}$ is exceeded. For argon as propellant, Hügel [11] gives an empirical value for the limiting current,

$$\frac{I^{*2}}{\dot{m}} \approx 2.5\ 10^{10} \qquad (\mathrm{A^2\ kg^{-1}\ s}),$$

which gives a current of the order of 12 kA for $\dot{m} = 6$ g/s. More recent work at Princeton and elsewhere has raised this by factors of up to 3, depending on the geometry and the injector configuration. An onset prediction based on the total starvation of the anode was proposed by Baksht, Moishes and Rybakov [3],

$$\frac{I^{*}m_i^2}{\dot{m}^4} = \frac{945}{8}\frac{ekT}{\sigma\mu_0^4}\frac{LH^8}{d^5}$$

which leads to a critical value of 19 kA for our geometry.

An explanation which does not include the Hall effect has been proposed by Lawless and Subramanian [19], based on the mechanism of an excessive back EMF induced by a strong convective effect $\mathbf{u} \times \mathbf{B}$ in the opposite direction of the applied driving field E. Neglecting the Hall effect they obtained, from a one-dimensional analysis, an expression for the limiting current:

$$\frac{I^{*2}}{\dot{m}} \approx 8.52\frac{a^*}{\mu_0} \qquad (\mathrm{A^2\ kg^{-1}\ s})$$

where a^* is the speed of sound at the choking point and μ_0 is the permeability of the vacuum. This gives a current of the order of 20 kA for $a^* = 10^4$ m/s and $\dot{m} = 6$ g/s. However the physical basis of their argument is open to criticism [22].

Assuming that the magnetic field is confined between two coaxial cylindrical electrodes and does not extend outside the exit plane of the thruster, one can integrate the effects of the Maxwell stress tensor, and one can predict the thrust due to the electro-magnetic effects by the formula:

$$T_{em} = \frac{\mu_0 I^2}{4\pi}\ln\frac{r_a}{r_c}$$

(11 Newton at 10kA for $\frac{r_a}{r_c} = 3$) The ratio $\frac{T_{em}}{\dot{m}}$ gives the exit velocity c_e.

The voltage is expected to be linear with the current for low currents (Joule heating), and to increase at a higher rate for high currents as the field accelerates the plasma and competes against the induced back EMF, showing a cubic dependence with the intensity.

Results

We have run fully coupled calculations for a mass flow rate of 6 grams per second and for various electrical currents between 0 and 10kA. Uncoupled calculations (i.e. calculating the electromagnetic field with a frozen flow field) have been obtained for currents between 0 and 100 kA.

A maximum of the magnetic field is observed along the cathode. Figure 2 shows the contours of constant rB. For an axisymetrical geometry these lines also represent the lines of current. The influence of the magnetic field on the conductivity tensor (Hall effect), is seen in the way the current lines concentrate at the tip of the anode and at the root of the cathode. As the current increases this effect becomes more pronounced. This effect can also be observed on figure 3, which shows the current density at the electrodes.

Figures 4 and 5 show the density contours for 0 and 10kA. For 10kA (figure 5) the density shows strong gradients and large fluctuations. At the inlet the density drops abruptly over a few cells. The compression of the plasma, under the influence of the Lorentz force (inward pinching effect), can be observed along the cathode and along the axis of symetry. Figure 6 shows an enlargement of the density plot for 10kA, where one observes: the compression of the plasma along the cathode; the strong rarefaction that follows the expansion of the plasma around the cathode corner, which reaches a minimum of $1.5\ 10^{19}\ m^{-3}$; the recompression along the axis of symetry, where the density reaches a maximum of $108.\ 10^{20}\ m^{-3}$ at a distance of 1 cm from the tip of the cathode. On the anode side the plasma expands monotonically from $33.\ 10^{20}\ m^{-3}$ to $0.15\ 10^{20}\ m^{-3}$. Figure 7 shows the density across the thruster along three different rows of cells. It shows the considerable increase in density in the cathode jet, downstream of the cathode along the axis of symetry.

A plot of the velocity vector obtained for 10kA (figure 8) shows a strong acceleration in the surface layer that surrounds the cathode. The existence of this layer can be inferred from the high values of both the electric field and the current density along the cathode (about an order of magnitude higher than at the anode).

The plot of the Hall number $\frac{B\sigma}{en}$ (figure 9) shows considerable gradients on the anode and cathode tips. These gradients are related to the electron density gradients created by the expansion of the plasma as it follows the electrode surfaces. The Hall effect (Tensorial conductivity) is likely to be responsible for the computational instabilities encountered at higher currents along the electrode surfaces.

The thrust was computed for various currents and is listed in table 2. The thrust increase due to the current is apparently very modest (9.8 N at 10kA), but is comparable to the thrust due to the Maxwell stress tensor predicted by the formula :

$$T_{em} = \frac{\mu_0 I^2}{4\pi} \ln \frac{r_a}{r_c}$$

(11 N at 10kA for $\frac{r_a}{r_c} = 3$). Thus the thruster is still operating at this condition mainly in the electrothermal regime.

Conclusions

The calculation of the MHD model was done for three values of the current: 0, 5kA and 10kA. The model does not converge above 10kA. The probable cause of the computational instability is the excessive value of the Hall parameter along the surfaces where rarefaction is present. Above a certain value of the current this rarefaction will be increased by the action of the Lorentz force, leading to a failure of the model along the boundaries.

The same cause may be responsible for the onset of instabilities observed in experimental devices. (The onset current expected from Hügel's formula is 12kA, the value from the Baksht et al. is 19kA, and the value from Lawless and Subramanian is 20kA).

The artificial damping introduced in the equation of motion in order to obtain a reasonably well-posed problem modifies the solution by an amount that reaches 5 percent of the momentum flux (for 10kA). The largest contribution to this error appears at the sharp turn around the anode corners.

References

[1] T. Ao, T. Fujiwara, "Numerical and Experimental Study of an MPD Thruster" *Proceeding of the 17th International Electric Propulsion Conference* Tokyo 1984, IEPC 84-08.

[2] G.V. Babkin, V.G. Mikhalev, S.N. Ogorodnikov, R.V. Orlov, A.V. Potapov, "High Current Coaxial Plasma Source", Sov. Phys. Tech. Phys. , Volume 20, 1975, pp 1175-1178.

[3] F.G. Baksht, B.Y. Moishes, A.B. Rybakov, "Critical Regime of a Plasma accelerator", Sov. Phys. Tech. Phys., Vol. 18, No. 12, June 1974, pp 1613-1616.

[4] R. D. Bühler "Plasma Propulsion for Near Earth Missions of Large Space Structures. Status, Problems and Prospects." Institut für Raumfahrtantriebe, Universität Stuttgart, IRA - 82 P 7

[5] I.S. Corry, R.G. Jahn, "Mass, Momentum and Energy Flow from an MPD Accelerator", Princeton University, Aerospace and Mechanical Sciences Report No. 999, 1971

[6] J.J. Dongara, C.B. Moler, J.R. Bunch, G.W. Stewart "LINPACK Users' Guide", SIAM.

[7] M. Drela, "Two-Dimensional Transonic Aerodynamic Design and Analysis Using the Euler Equations", GTL Report No. 187, Massachusetts Institute of Technology, February 1986.

[8] M.B. Giles, "Newton Solution of Steady Two-Dimensional Transonic Flow" PhD Thesis, Department of Aeronautics and Astronautics, MIT, June 1985.

[9] J.M.Hoell, J. Burlock, O. Jarrett, "Velocity and Trust Measurements in Quasi-Steady Magneto-Plasma-Dynamic thruster", AIAA paper No. 70-1080.

[10] H. Hügel, Flow Rate Limitations in the Self-Field MPD Accelerator", AIAA paper No. 73-1094.

[11] H. Hügel, "Zur Funktionsweise der Anode im Eigenfeldbeschleuniger", Deutsche Forschungs- und Versuchsanstalt für Luft- und Raumfahrt, DFVLR-FB 80-20

[12] R.G. Jahn, "Pysics of Electric Propulsion", Chapters 8 and 9, McGraw-Hill, 1968.

[13] R.G. Jahn, A.J. Kelly, "Quasi-Steady Magnetoplasmadynamic (MPD) Thruster Performance Development", Princeton University, Department of Mechanical Engineering and Applied Science, MAE Report No. 1567, March 1983.

[14] A. Jameson, W. Schmidt, E. Turkel, "Numerical Solution of the Euler Equations by Finite Volume Methods Using Runge-Kutta Time-Stepping Schemes." AIAA-81-1259

[15] A. Jameson, S. Yoon, "Multigrid Solution of the Euler Equations Using Implicit Schemes", AIAA paper No. 85-0293.

[16] D. C. Jespersen, "Recent Developments in Multigrid Methods for the Steady Euler Equations", Von Karman Inst. for Fluid Dynamics, CFD Volume 2 1984.

[17] I. Kimura, K. Toki, M. Tanaka, "Current Distribution on the Electrodes of MPD Arcjets", AIAA Journal, Vol. 20, No. 7, July 1982.

[18] K. Kuriki, H.Suzuki, "Thrust Measurment of Quasi-Steady MPD Arcjet", AIAA paper No. 76-1002.

[19] J.L. Lawless, V.V. Subramanian, "A Theory of Onset in MPD-Thrusters, AIAA paper 85-2039.

[20] H. Lien, R.L. Garrison, " System Trade-offs for Pulsed MPD Thruster in Space Mission Application ", AIAA paper No. 72-457.

[21] A.C. Malliaris, R.R. John, R.L. Garrison, D.R. Libby "Quasi-Steady MPD Propulsion at High Power", NASA CR-111872.

[22] M. Martines-Sanches, "Structure of Self Field Accelerated Plasma Flows", AIAA paper 87-1065.

[23] R. Peyret, T. D. Taylor," Computational Methods for Fluid Flow", Springer Verlag, pp 108-112.

[24] T.H Pulliam, J.L. Steger, "Recent Improvements in Efficiency, Accuracy and Convergence for Implicit Approximate Factorisation Algorithms", AIAA Paper No 85-0360.

[25] R.P. Reklis, R.J. Conti, "Computational Probing of Hypersonic Laminar Wake", AIAA Paper No. 84-1579.

[26] P.J. Roache, "On Artificial Viscosity", Journal of Computational Physics, Vol.10, No.2, October 1972.

[27] M. Tanaka, I. Kimura, Y. Arakawa, "Current Distribution on the Electrodes of MPD Arcjets with Applied Magnetic Field", AIAA Paper, No. AIAA-82-1918, 1982

[28] M. Tanaka, I. Kimura, "Theoretical Analysis of Current Distribution and Plasma Acceleration in MPD Arcjet" *Proceeding of the 17th International Electric Propulsion Conference* Tokyo 1984, IEPC 84-07.

[29] P.J. Turchi, R.G. Jahn, "The Cathode Region of a Quasi Steady MDP Arcjet", AIAA Paper No. 70-1094.

Symbols

a^*	Speed of sound at chocking point in the theory of Lawless and Subramanian
B	Magnetic field (T)
c_e	Exit velocity
C_l	Non dimensional parameter in the energy equation (Clausius Number)
d	distance between electrodes
e	Charge of the proton
E	Electric field ($V\ m^{-1}$)
E_{EM}	Electromagnetic energy per unit volume
E_I	Internal energy per unit volume
E_K	Kinetic energy per unit volume
H	Average perimeter of the inlet
H_e	Hall parameter
I^*	Current at the threshold of the turbulent regime.
J	Current density ($A\ m^{-2}$)
k	Boltzman constant
L	Average length of the channel
m_i	Molecular mass of the gas (kg)
$\overline{\overline{M}}$	Maxwell stress tensor ($N\ m^{-2}$)
$\dot{m}$	Mass flow rate of the propellant ($kg\ s^{-1}$)
m_z, m_r	Z- and r-momentum ($= \rho u_z, \rho u_r$)
n_e	Density of electrons (m^{-3})
P	Pressure ($N\ m^{-2}$)
q	Heat flux ($W\ m^{-2}$)
R	Gas constant ($J\ kg^{-1}\ K^{-1}$)
R_m	Magnetic Reynolds number
$\overline{\overline{S}}$	Stress tensor ($N\ m^{-2}$)
T	Temperature (K)
u	Velocity ($m\ s^{-1}$)
$\overline{\overline{uu}}$	Diad ($u_i u_j$ in cartesian coordinates)
β	Plasma-Beta (pressure/magnetic pressure)
γ	Specific heat ratio
κ	Heat conductivity
μ_0	Permittivity of vacuum
ρ	Mass density ($kg\ m^{-3}$)
σ	Conductivity ($Si\ m^{-1}$)
τ_e	Electron collision time
ϕ	Axisymertic coordinate
ω_{ce}	Electron gyrofrequency (angular)

Cathode radius	r_c	2. cm
Anode radius	r_a	6. cm
Cathode length		6. cm
Anode length		12. cm
Inlet density	ρ_{inlet}	$2.21\ 10^{-4}$ kg m^{-3}
Inlet pressure	P_{inlet}	1144 Pa
Inlet velocity	Uz_{inlet}	2700 m/s
Inlet X-sec. area	A_{inlet}	10^{-2} m^2
Temperature	T_0	$1.25\ 10^4$ K
Conductivity	σ_0	$3.8\ 10^3$ Si/m
Mass flow rate	$\dot{m}$	6 g/s
Current	I	(0., 5., 10.) kA
Gas constant	R	0.416 kJ/kg/K

Table 1: Parameters for the Calculations

RESULTS OF THE MODELS

Current (kA)	Voltage MHD model (V)	Thrust (MHD) (N)	Isp (MHD) (km/s)
0.		30.2	5.0
5.	6.7	32.2	5.4
10.	16.2	40.	6.7

Table 2: Results

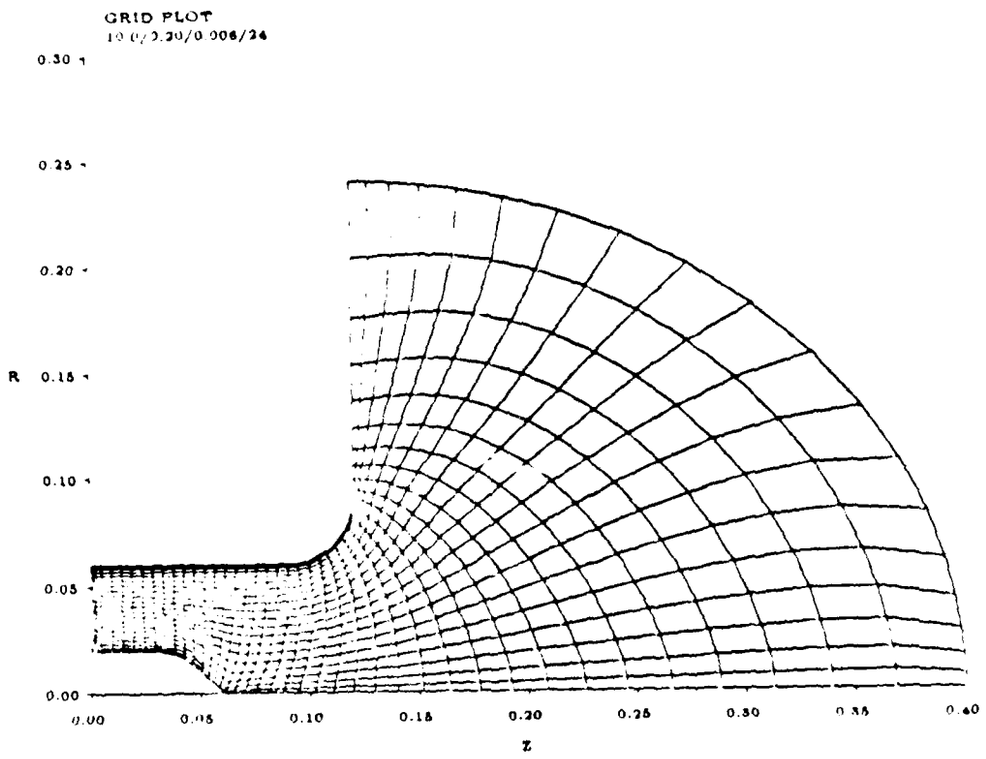

Figure 1: Grid

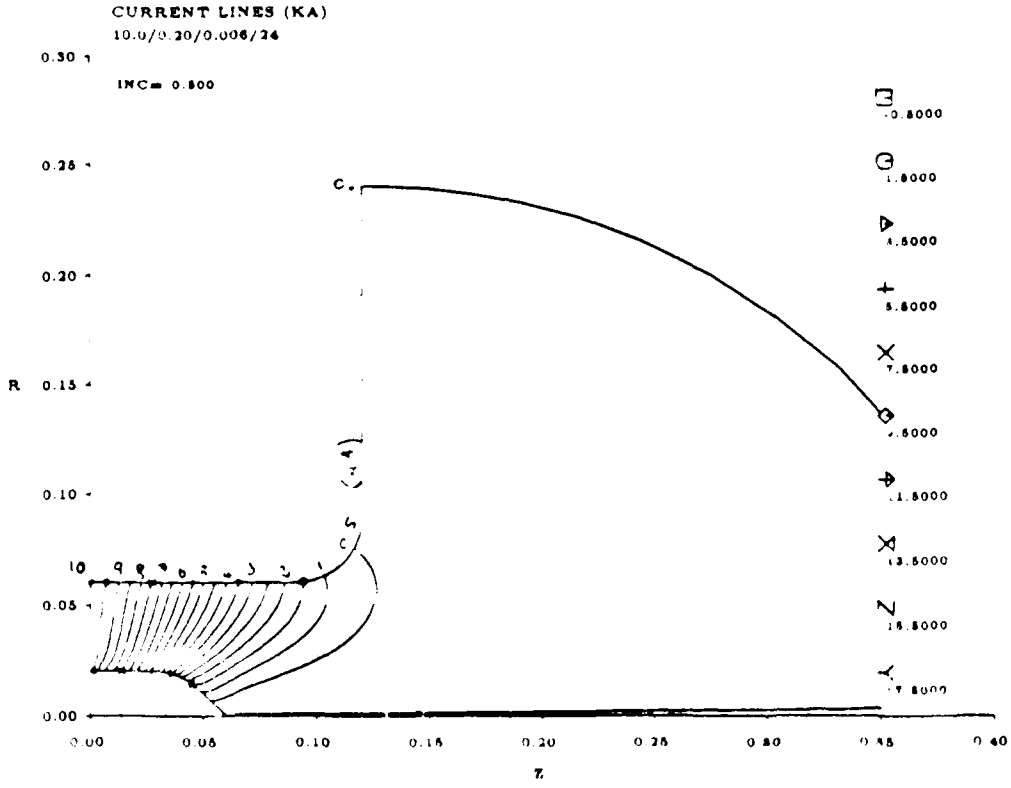

Figure 2: Current lines for $I = 10kA$ (Calculation)

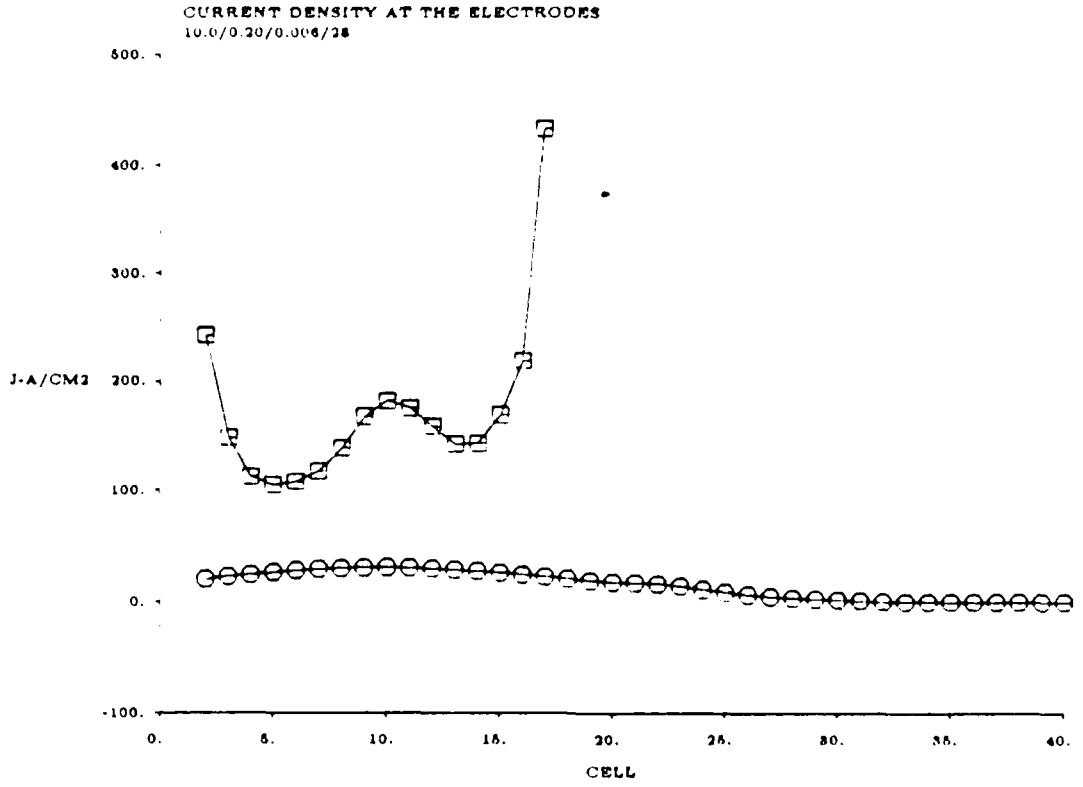

Figure 3: Current density at the electrodes for $I = 10kA$ (Calculation)

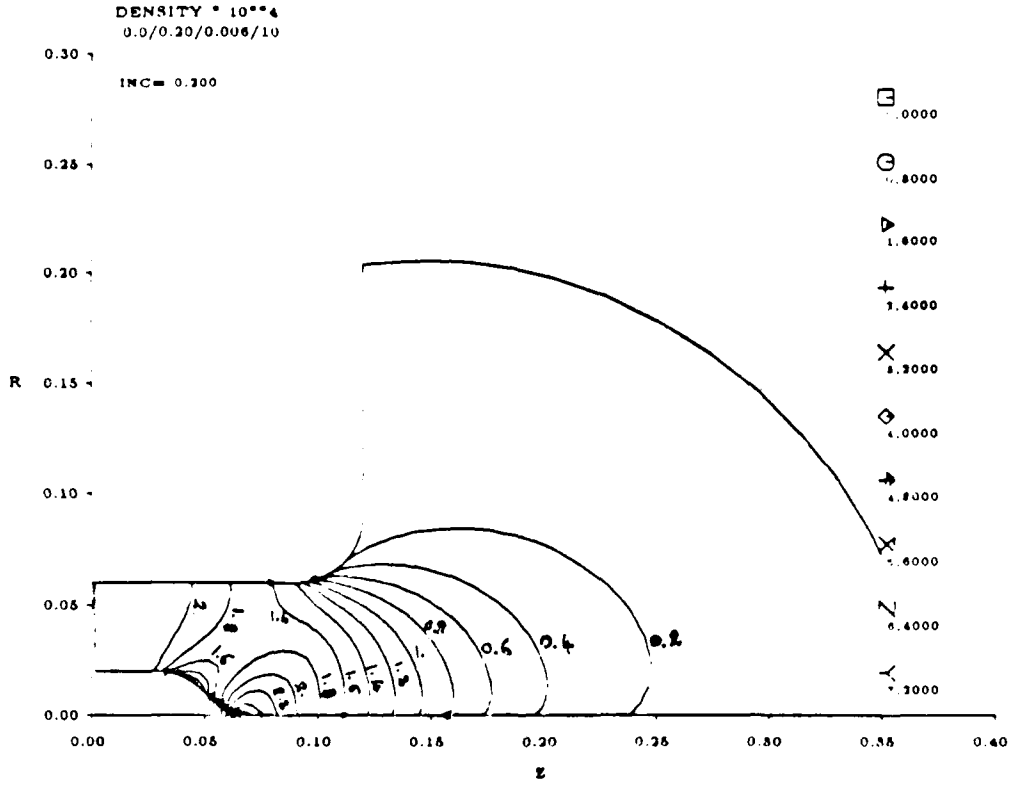

Figure 4: Density for $I = 0kA$ (Calculation)

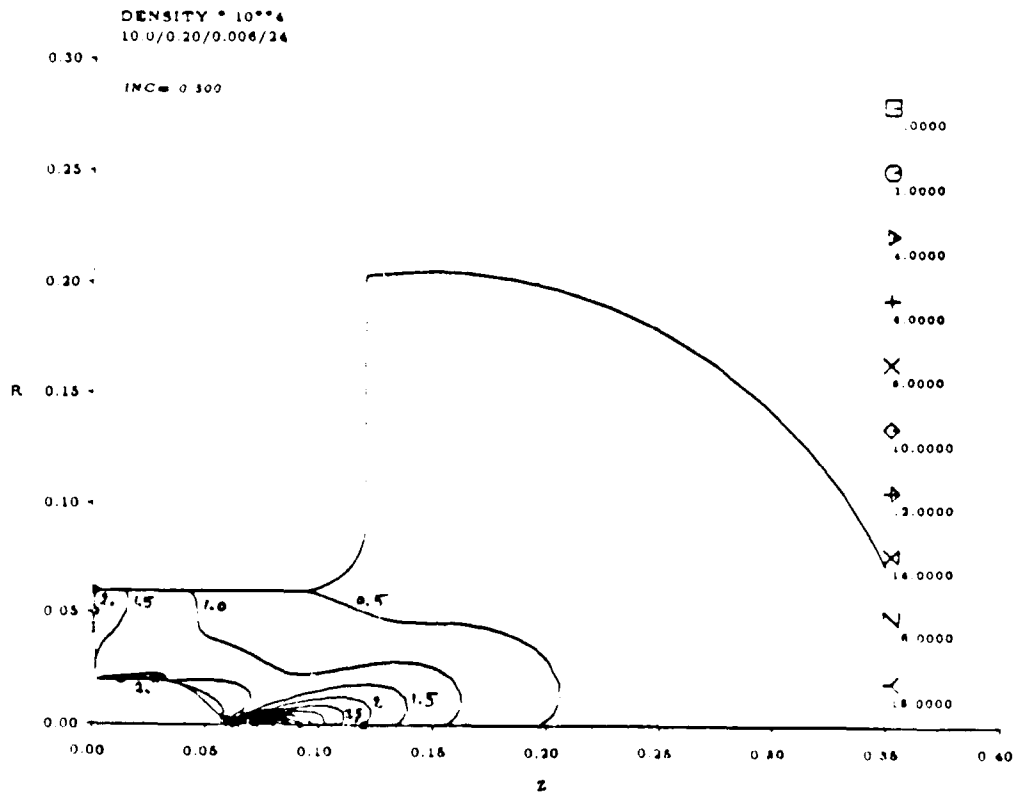

Figure 5: Density for $I = 10kA$ (Calculation)

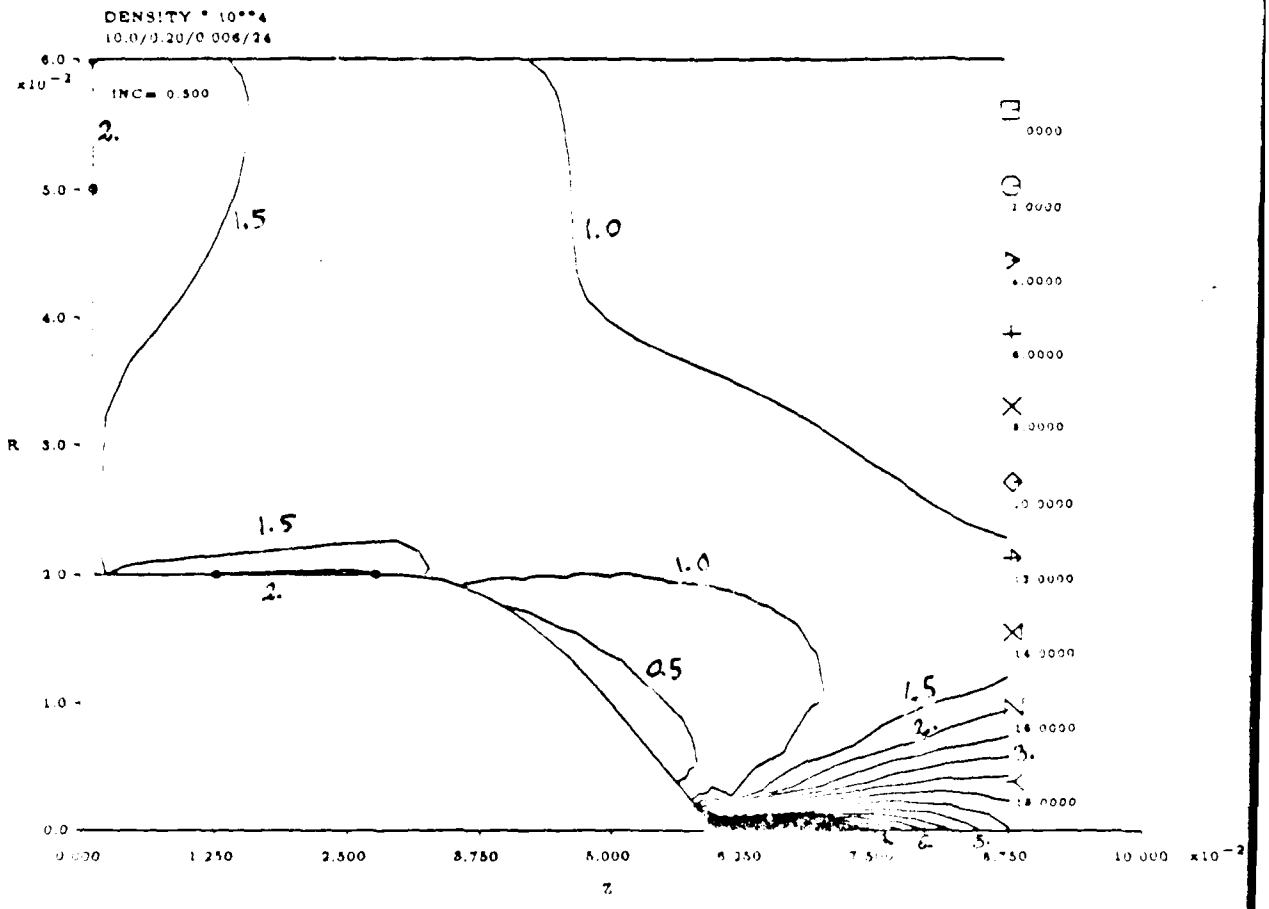

Figure 8: Density for $I = 10kA$ (Calculation)

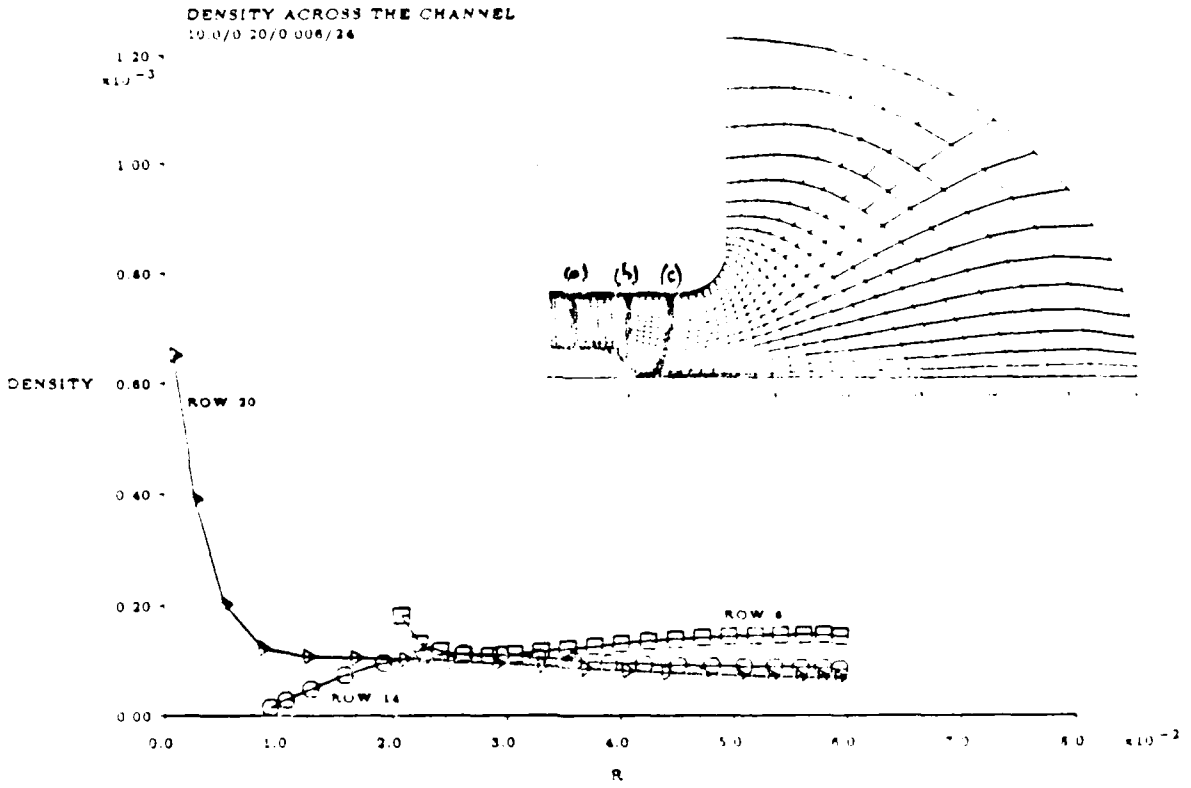

Figure 7: Density across the channel for $I = 10kA$ (Calculation) (a) 6th row of cells (inside the channel); (b) 14th row of cells (end of the cathode); (c) 20th row of cells (beyond the tip of the cathode).

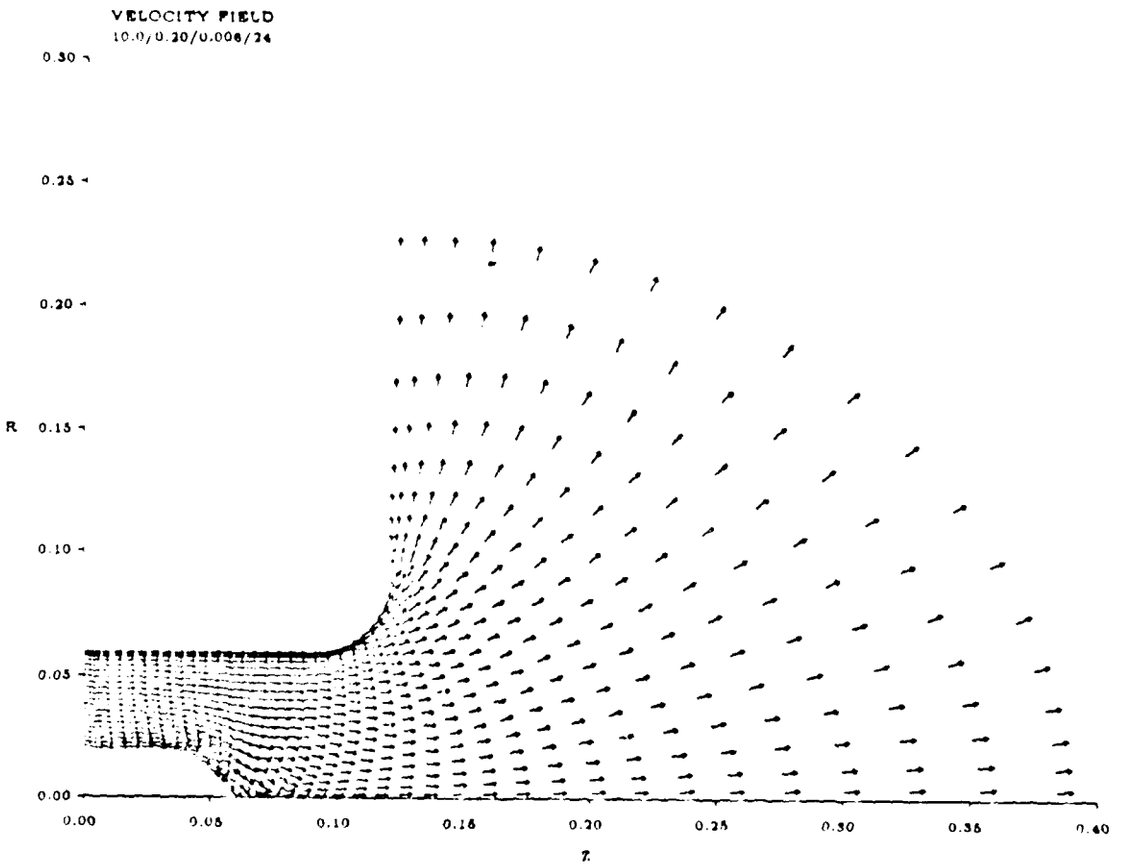

Figure 8: Velocity vectors for $I = 10kA$ (Calculation)

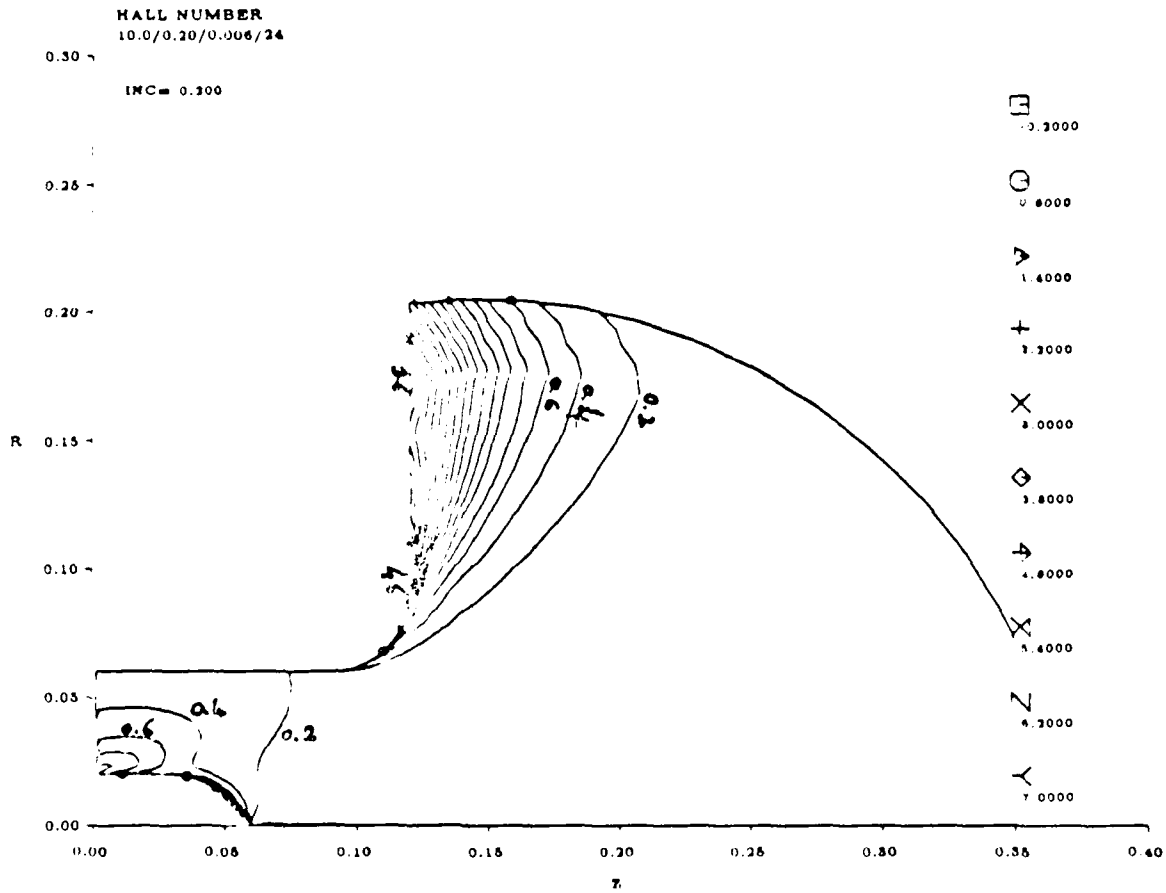

Figure 9: Hall number H_θ for $I = 10kA$ (Calculation)

APPENDIX III

AIAA-87

AIAA-87-0998
Effect of Axial Variation of Electrode Spacing on MPD Arcjet Behavior

D. J. Heimerdinger and M. Martinez-Sanchez,
Massachusetts Institute of Technology,
Cambridge, MA;
J. F. Davis and P. J. Turchi,
RDA Washington Research Lab,
Alexandria, VA

AIAA/DGLR/JSASS 19th International
Electric Propulsion Conference
May 11-13, 1987
Colorado Springs, Colorado

AIAA-87-0998 EFFECT OF AXIAL VARIATION OF ELECTRODE SPACING ON MPD ARCJET BEHAVIOR

D. J. Heimerdinger and M. Martinez-Sanchez
Massachusetts Institute of Technology
Space Systems Laboratory
Cambridge, Massachusetts 02139
J. F. Lewis and P. J. Turchi
RDA Washington Research Laboratory
Alexandria, VA 22314

Abstract

Two annular magnetoplasmadynamic (MPD) thrusters were constructed and operated in a regime where anode starvation processes limit the thrusters' performance. Magnetic field and floating potential measurements were conducted to determine the operational differences between a channel with constant interelectrode separation and a channel with an initial constant separation and a divergent exit. The channel with the constant electrode separation shows evidence of strong concentrations of current at both inlet and exit, along with strong indications of accompanying electrode erosion. In the divergent section, current densities were greatly diminished with decreased evidence of ablation. Evidence tends to indicate that electrode erosion is unavoidable for a starved anode; however, through spatial variation of the interelectrode spacing local ohmic heating can be controlled to minimize ablation of the other components, such as the cathode and backplate insulator.

Nomenclature

a	magnetoacoustic speed
$\vec{B}$	magnetic induction field
$\vec{E}$	electric field
F	thrust
J	total current
$\vec{j}$	current density
$\dot{m}$	mass flow rate
R	gas constant
r_a	anode radius
r_c	cathode radius
T	plasma temperature
$\vec{u}$	mean mass velocity
β	Hall parameter
γ	specific heat ratio
μ_0	permeability of free space
σ	plasma scalar conductivity

Introduction

The goal of the designer of an MPD arcjet is to obtain desirable overall performance. To achieve this goal, it is useful to manipulate internal distributions of current density and mass flow. In a previous paper, Martinez-Sanchez and Heimerdinger derived an approximate two-dimensional hydrodynamic MPD arcjet model which indicated that the performance and the internal distributions of the previously described quantities can be manipulated by an axial variation of the interelectrode separation.[1] This paper presents preliminary data from an experiment based on the analysis from reference 1.

MPD arcjets can be distinguished from other electric thrusters by their use of the $\vec{j}\times\vec{B}$ Lorentz force as their primary source of thrust. An approximate overall thrust equation shows this feature by the quadratic behavior of the thrust with the applied current and a weak dependence on geometry.[2]

$$F = \frac{\mu_0 J^2}{4\pi} \left(\ln \frac{r_a}{r_c} + \frac{3}{4} \right)$$

For a given thruster geometry and mass flow rate, the efficiency also increases with current because of the transition from electrothermal acceleration due to the ohmic heating of the plasma to primarily an electromagnetic acceleration. Unfortunately, an operational limit called "onset" is reached where both erosion of the thruster and overall voltage have been noted to increase dramatically. The term onset originated from the appearance of megahertz terminal voltage oscillations which quickly grow in amplitude. Sutton defined onset as that level where voltage oscillations reach 10% of the average terminal voltage.[3] In a given geometry, the onset limit scales approximately with the parameter $J^2/\dot{m}$ and this correlates with the exhaust velocity.[4,5]

In reference 1, the appearance of onset is attributed to an anode starvation phenomenon caused by axial deflection of the local current vector by the Hall effect. In figure 1, the Lorentz force, which is orthogonal both to the magnetic induction field and the current density vector, has a component directing the plasma towards the cathode. As the plasma adjacent to the anode becomes rarefied, deflection of the current vector is exacerbated as the Hall parameter grows due to the local decrease in collisionality. The region adjacent to the anode, increases in voltage to attract electrons and ensure current flow. Eventually the magnitude of this potential grows large enough for electrical breakdown to occur which allows concentrated arcs to form on the anode. This effect is intrinsic to MPD arcjet operation unless an external electric field is applied to halt the growth of axial current.

In addition to plasma depletion at the anode at high currents and low mass flow rates, the MPD arcjet can operate at a significant magnetic Reynolds number which implies a tendency towards convection of the magnetic field with the plasma. Such convection tends to produce strong concentrations of current at the entrance and exit, due to the presence of a low back

This work was supported by the Air Force Office of Scientific Research under grant number AFOSR-86-0119D.

electromotive force (emf). From Ohm's law,

$$\vec{J} + \vec{J}\times\vec{B} = \sigma(\vec{E} + \vec{u}\times\vec{B})$$

the plasma must take the entire electric field in the absence of back emf, thus forcing strong current concentrations to occur. Because of this, local heating of the insulator and electrodes occurs, accounting for their associated ablation.

The aim of this paper is to present data from an experiment based on a theory that claims the ability to control the distribution of the magnetic field, hence current density, in an MPD arcjet channel through careful axial variation of the interelectrode separation.

The Experimental Apparatus

A joint experiment between MIT and RDA Washington Research Laboratory in Alexandria, Virginia was conducted at the RDA facilities. A 400 kJ capacitor bank was modified into an eight stage LC ladder network to provide a flat quasi-steady current pulse to the MPD arcjet. The bank has a total capacitance of 2.0 mF where each section is separated by a 10 μH solenoid inductor. The pulse forming network (PFN) is designed with a high voltage ignitron switch at each stage so that the output waveform can be modified depending on the sequencing of ignitrons (refer to figure 2). If a single ignitron (ignitron #8) is fired, the resulting waveform has a duration of about 0.8 ms. This system requires a matched load of 0.2 Ω providing a maximum safe current pulse of 32 kA to the MPD arcjet. If ignitrons #1 and #8 are fired simultaneously, the impedance of the bank drops in half and a pulse of about 0.45 ms is achieved. With this configuration, a maximum safe current level of 55 kA can be supplied to the arcjet.

The PFN is connected to the arcjet, which is situated in a cylindrical stainless steel vacuum tank 6 m long and 0.6 m in diameter. The vacuum is maintained at a static level of $< 10^{-4}$ torr by two six inch diffusion pumps. The tank and associated pumps are electrically floating to prevent spurious alternate current paths for the PFN-arcjet circuit. The MPD arcjet assembly drawing in figure 3 shows the relation of its various components. The exterior of the arcjet is constructed as an anode sleeve which is isolated from the vacuum tank by a Plexiglas flange. The sleeve and the outer portion of the anode are hardcoat anodized with a 2 mil layer to inhibit current attachment beyond the anode lip. The cathode and mass injection assemblies both slide into the anode sleeve. A boron nitride insulator, seated in a Plexiglas assembly, isolates the anode from the cathode while a Mylar film and tape jacket surround the cathode sleeve completing the anode/cathode insulation. By constructing the feeds to the arcjet in this coaxial manner, the parasitic inductance of the device is kept to a minimum.

Mass is provided to the channel from a large reservoir placed close to the MPD arcjet channel. Six valves feed a preexpansion chamber directly upstream of 48 choked orifices. The gas flows through the choked orifices and expands through a boron nitride insulator, which also has 48 larger diameter holes, into the channel.

The anode is made of aluminum, primarily for its machinability, low weight, and low cost. The cathodes are made from copper primarily for its electrical properties, and it is both less expensive and easier to machine into the required geometries than other more desirable materials.

A Tektronix data acquisition system is utilized for data collection, manipulation, and analysis. It is kept inside a large Faraday cage for shielding against stray electromagnetic noise. A block diagram of the MPD thruster system is seen in figure 4.

Initiation of the discharge occurs after the bank is charged to the appropriate operating value. At this point, the valves are opened with a 3 kV pulse and are held open until the required steady state mass flow rate is reached. After this delay (approximately 10 ms), the required ignitrons are triggered, several kilovolts appear across the electrode gap, breakdown ensues, and, after a short transient period (typically 100 μs), quasi-steady operation is reached.

Thruster voltage is measured by a 1000:1 Tektronix voltage probe optically isolated from the data acquisition system. Floating potential is measured relative to the anode from a simple Langmuir probe through a 20:1 voltage divider. The floating potential probe is constructed primarily from a short piece of thin tungsten wire. The total current is measured by a large Rogowski loop surrounding the cathode sleeve at the base of the power connection. This probe measures the time rate of change of the enclosed magnetic flux, which is integrated to give the magnetic field, and, from Ampere's law, the total enclosed current. An active integrator with a 377 μs integration time constant and a 70 ms associated droop time is used with this Rogowski loop. Enclosed current, at points inside the plasma, is measured from a small 20 turn Rogowski loop enclosed in a long Pyrex tube. Again, an active integrator with a 3.39 μs integration time constant and a 70 ms associated droop time is used to integrate the time derivative of the magnetic induction (e.m.f.).

For this experiment, the bank was fired with #1 and #8 ignitrons so that an operating point of 50 kA at 4.2 g/s of Argon was obtained.

Two MPD arcjet channels were constructed and diagnosed. A constant area channel consists of a cylindrical anode and concentric cathode with a constant interelectrode separation of 1.9 cm. A second channel, the modified flared channel, was based on a calculation from the theory in reference 1 for uniform current density distributions along the electrodes. To minimize cylindrical effects, the annular channel geometry was based on a large cathode diameter compared to the interelectrode gap. For a mass flow rate of 4.2 g/s of Argon at an operating point of about 50 kA, a channel with the area variation shown in figure 5 is predicted by the theory. In order to examine the behavior of the two channels, we chose to operate in the vicinity of onset, where onset is predicted by the theory as the solution where zero density is encountered somewhere along the anode. The design theory, for which this calculation is based, neglects the initial ionization processes that occur in a region of the discharge dominated by ohmic heating where large changes in plasma velocity and density occur.[4] For this reason, a low speed near the entrance for a given mass flow rate leads to large variations in the interelectrode separation. This is immediately seen in figure 5 at the channel entrance upstream from the point of minimum area. However, for this experiment, in order to ensure reliable ignition at the inlet, only the portion

downstream from the point of minimum area was flared. The upstream portion remains fixed at 1.8 cm. Hence this device is called the modified flared channel. In both geometries, the anode remains the same and all channel variation is taken by the cathode. This is done for simplicity in the machining of the electrodes.

Results and Discussion

Both channels were probed to determine current and floating potential distributions. Typical probe responses are seen in figures 6 and 7. The enclosed current and floating potential contours for the two channels are found in figures 8 and 9 respectively. Determination of the plasma potential from floating potential measurements necessitates knowledge of the electron temperature and and ionic species.[7] Other work has shown that this temperature variation is small so that the differences in floating potential is sufficient for the calculation of electric fields.

In both channels, large axial currents are found in the anode region. This implies large local values of the Hall parameter. From the floating potential contours, there also appears to be a large positive potential drop at both anodes. A large Hall parameter implies a a deficiency of charge carriers which correlates with the large positive anode fall required to pass all of the current. Based on reference 1, it is apparent that both channels are operating beyond the onset level.

Typical terminal voltage traces do not display the high frequency oscillations that typically characterize onset. Megahertz voltage oscillations are seen, however, in the floating potential characteristics. Terminal voltage scaling shown in figure 10 does not display the cubic dependence of voltage that one would expect to precede onset.[1,8]

Turchi suggests that an increase in ablation as the exhaust speed exceeds the Alfven critical speed, based on ablation energy, may preclude a cubic dependence of voltage on current in MPD arcjet operation, even if the dominant acceleration mechanism is electromagnetic.[9]

Examination of both thrusters shows strong evidence of ablation. Both anodes show erosion primarily at their exit lip. Both cathodes also show erosion, especially in the entrance region. In fact, after less than 100 discharges, copper from the cathode is plated on the boron nitride insulating injector plate. The anode wear is similar in both geometries, however, the cathode wear is markedly different. For the constant area channel, bands about a half a centimeter wide are seen at both the entrance and the exit. The band at the entrance looks like freshly machined copper, indicative of strong and even erosion. The band at the exit is well defined but is not quite as clean as the one at the entrance. The band at the entrance are largely composed of semicircular clean regions adjacent to the mass injection sites. More clean spots are noted about a half to one centimeter further downstream directly in line with the mass injection holes in the boron nitride insulator. The remaining cathode shows strong evidence of fine line arc structures extending from the cathode downstream end almost to the cathode root. These fine structures are branch-like and tend to branch in an upstream direction.

In the modified flared channel, the clean band at the exit is absent, but there is a wide clean band at the entrance between 0.75 cm to 1.3 cm in extent. Unlike the other bands, this one has a very poorly defined downstream edge. The fine line structures are completely absent on this cathode. Drawings of both cathodes are found in figures 11 and 12.

Figure 13 shows a graph of the current density along both cathode surfaces. In both cases, strong concentrations are found in the initial portion of the channel. In the constant area channel, the current density drops to a low value at mid-channel and then increases dramatically near the exit. The current density in the modified flared channel remains high until just before the beginning of the flared region where it subsequently drops significantly below the level found in the constant area channel.

The theory tends to support the trends seen in figure 13. At the channel entrance, the plasma is moving slowly so the back emf is low. In both channels, the interelectrode distance at the entrance is the same, and both plasmas must take the total electric field in the absence of any significant back emf. At the exits the magnetic field drops towards zero and once again the back emf is small. In this region, the plasma once again must take the total electric field. However, in the modified flared channel, the local electric field decreases due to the increased interelectrode separation, so a strong current concentration is mitigated. Since the current density is lower in the flared region, and the same current is passed as in the constant area channel, the current density in the upstream portion of the modified flared channel must increase. This may account for higher ohmic heating which may lead to an elevated plasma temperature, and therefore higher ionization fraction and electrical conductivity, in the modified flared channel.

The theory also indicates that high magnetic Reynolds number flows in constant area channels tend to have strong current concentrations at the exit as the magnetic field goes to zero. Also it shows that the magnetic field in a flared channel is more evenly distributed due to the controlled plasma expansion and the convection of the magnetic field with the fluid at higher magnetic Reynolds numbers. In this operating regime, the magnetized plasma behaves analogously to an ordinary compressible gas except that the speed of sound is replaced by the magnetoacoustic speed, defined as

$$a = \sqrt{\gamma RT + \frac{B^2}{\mu_0 \rho}}$$

which is a combination of the speed of sound and the Alfven speed.

Data for the constant area channel does not seem to exhibit this behavior. The theory neglects the effect of viscosity which may account for some of the differences. In this channel, the presence of a large axial component of the current acts to deplete the anode and pressurizes the cathode. The moving plasma, blocked by the cathode must move along it, which may be sufficient for viscous dissipation to slow the plasma. If the plasma speed is sufficiently lowered, the corresponding magnetic Reynolds number for the arcjet may be low enough for a more uniform axial decrease of magnetic field. If the magnetic field is sufficiently low at the exit,

ordinary gas dynamic choking can occur (as in the case of ordinary gas dynamics with Fanno flow for flows with friction and Rayleigh flow for flows with heating), thus limiting the effective exhaust velocity to that corresponding to Mach 1.

However, the modified flared channel does exhibit some of the trends anticipated by the theory. Although pressurization of the cathode is evidenced by the current contours, the flaring of the cathode tends to reduce the obstruction of the plasma motion. Also, an increased plasma temperature can lead to a strong drop in plasma viscosity as shown in figure 14.[10] This could act to sufficiently lower the viscous losses expected in this region. Therefore, the magnetic Reynolds number may not be reduced significantly; in fact, the thermodynamic expansion encountered in the nozzle region would allow for an increase in the plasma velocity beyond the appropriate sonic or magnetoacoustic speed, which would translate to an increase in the magnetic Reynolds number.

This is further evidenced by the difference in the terminal voltages measured in the arcjets. Martinez-Sanchez shows that the terminal voltage decreases with increasing magnetic Reynolds number.[1] In this experiment, the constant area channel is seen to operate at a mean voltage of 78.1 ± 1.5 volts, while the modified flared channel operates at 70.3 ± 1.8 volts.

The plasma discharge near the anode appears quite different from the cathode. The anode current densities and voltage drops are plotted in figure 15. Both geometries exhibit large potential drops indicative of starved anodes. For the most part, the magnitude of the voltage drop follows the magnitude of the current density. The only place where there is a deviation from this behavior is at the entrance to the modified flared channel. Here, high current density is associated with a low voltage drop. This tends to suggest the development of concentrated arcs, substantiated through examination of the anode.

In this initial region, there is a high demand to pass current due to the low back emf, but the gas has a low conductivity since it has not yet become fully ionized. The local electric fields may not yet be sufficient to support a diffuse discharge so the plasma may have no other choice but to arc strongly and locally heat the plasma. As the plasma is convected downstream, its conductivity increases, and the arc may become more diffuse. Eventually, no severe arcing is necessary, as the conductivity and the back emf have risen to a level so that a more diffuse discharge may be supported. This is evidenced by the wear pattern on the inside of the anode. Arcing, adjacent to the injectors at the anode, is seen with tracks that appear to continue downstream. As the arcs continue downstream, they appear to broaden and weaken until the wear on the anode surface becomes more azimuthally uniform. This occurs about a third of the way down the anode from the channel entrance.

Significant erosion can occur in other areas of the MPD arcjet for reasons that are not necessarily associated with anode current conduction onset. In this experiment, erosion of the cathode has been locally decreased by flaring the cathode. Theory suggests that this is also valid for the entrance region.[1] By decreasing the local electric field, the current is spread out, thereby decreasing its density and the associated local ohmic heating. This not only protects the cathode, but the insulator region as well.

Conclusion

Preliminary examination of data from an MPD arcjet experiment has shown that arcjet operation can be modified through a variation of the interelectrode separation. Further experimentation should be done to study the effect of increasing the interelectrode distance at the entrance in a similar manner as was done at the exit to alleviate the high concentration of current along the cathode. If the expected decrease in current density is encountered, additional experimentation using better cathode materials with superior ablation properties such as thoriated tungsten or barium oxide impregnated tungsten [11] should be done, as well as continued study of the MPD arcjet plasma properties so as to understand loss mechanisms such as friction in the MPD arcjet. And finally, additional experimentation should be conducted to study the thruster operation below onset.

References

1. Martinez-Sanchez, M. and Heimerdinger, D.J., "Two-Dimensional Analysis of an MPD Arcjet," AIAA-85-1130 presented at the AIAA/DGLR/JSASS 19th International Electric Propulsion Conference, Sept. 30 - Oct. 2, 1985, Alexandria, VA.
2. Jahn, R.G., Physics of Electric Propulsion, McGraw Hill Book Company, New York, 1968.
3. Rudolph, L.K., and Jahn, R.G., "The MPD Thruster Onset Current Performance Limitation," Ph.D. Dissertation, Princeton University, Princeton, NJ, MAE Report No. 1492, September 1980.
4. King, J. W., Smith, W. W., Jahn, R.G., and [illegible], K. E., "Effect of Thrust Chamber Configuration on MPD Arcjet Performance," Proceedings of the Princeton/AIAA/DGLR 15th International Electric Propulsion Conference.
5. Malliaris, A. C., John, R. R., Garrison, R. L., and Libby, D. R., "Performance of Quasi-Steady MPD Thrusters at High Powers," AIAA Journal, Vol. 10, No. 2, February 1972.
6. Martinez-Sanchez, M., "The Structure of Self-Field Accelerated Plasma Flows," AIAA-87-1065 presented at the 19th AIAA/DGLR/JSASS International Electric Propulsion Conference, May 11-13, 1987, Colorado Springs, CO.
7. Huddlestone, R. H. and Leonard, S. L., Plasma Diagnostic Techniques, Academic Press, New York, N.Y., 1965.
8. Ho, D. D., Jahn, R. G., "Erosion Studies in an MPD Thruster," Masters Thesis, Princeton University, Princeton, NJ, MAE Report No. 1545, May 1982.
9. Turchi, P. J., "Critical Speed and Voltage-Current Characteristics in Self-Field Plasma Thrusters," Journal of Propulsion and Power, Vol. 2, Sept-Oct. 1986, pp. 498-503.
10. Rose, D. W. W. and Clark, M. J., ed., Plasma and Controlled Fusion, Volume 1, Electrical Discharges, Academic Press, New York City, 1961.
11. Tamatsu, K., Mori, K., Kuninaka, H., and Kuriki, K., "Effect of Electrode Configuration on MPD Arcjet Performance," Paper ISTC 84-11 presented at the 15th AIAA/DGLR/JSASS International Electric Propulsion Conference, Tokyo, Japan, 1984.

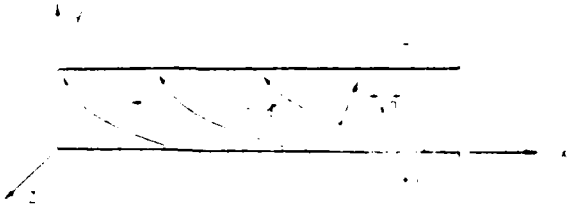

Figure 1 MPD Accelerator Geometry

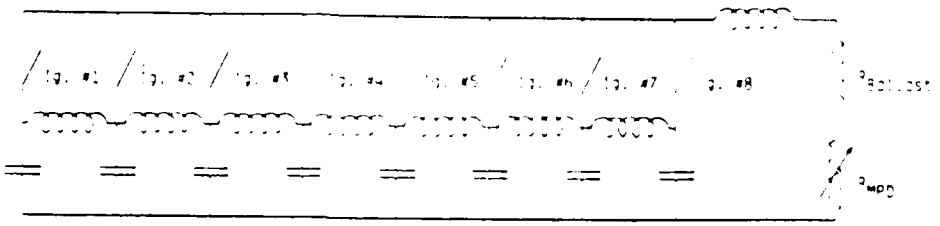

Figure 2 Pulse Forming Network Schematic

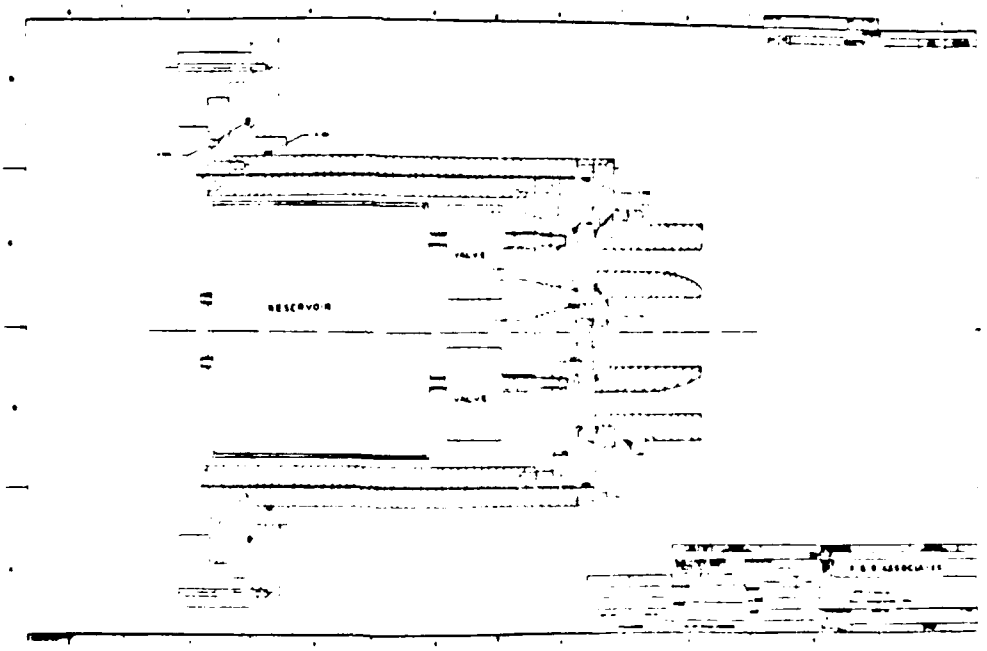

Figure 3 MPD Accelerator Assembly Drawing

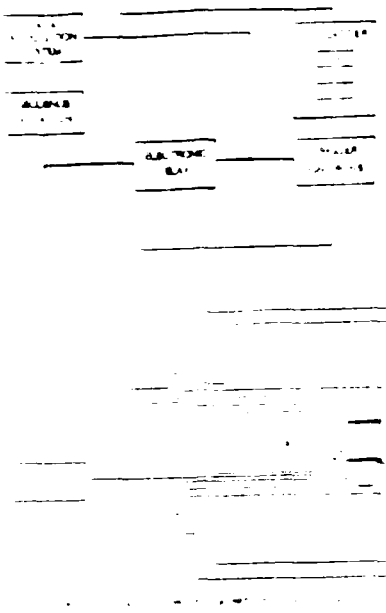

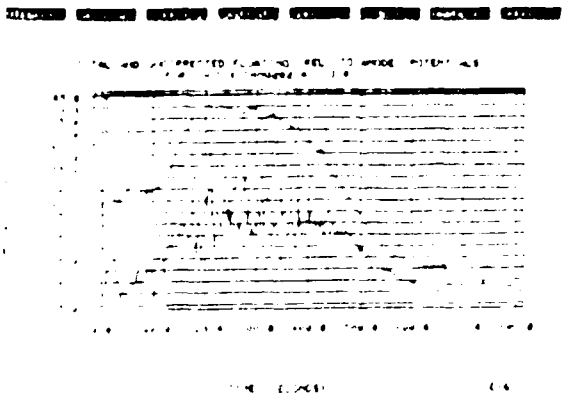

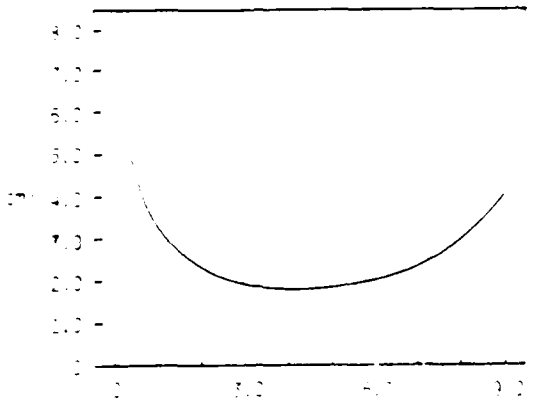

Figure 5. Calculated interelectrode separation for
I_p = 50 kA, $\dot{I}_p$ = 4.0 G/s

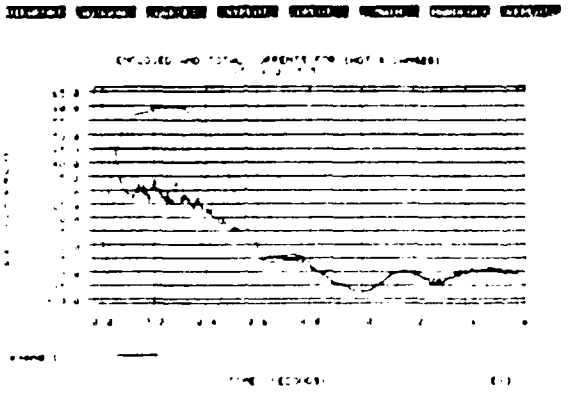

Figure 6. Typical Enclosed and Total Current Oscilloscope Traces

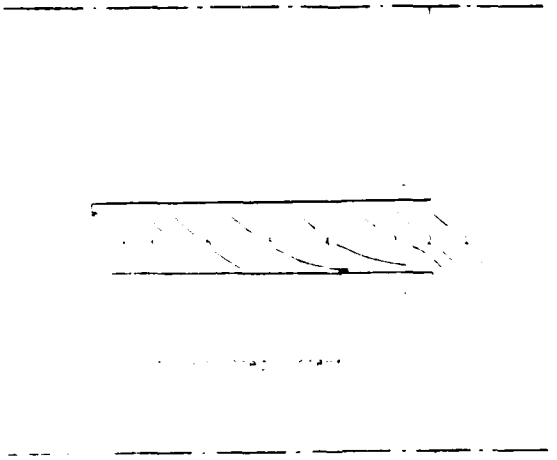

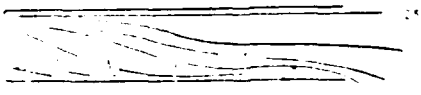

Figure 8. Enclosed Current Signal Showing Pattern of Transient Arc Phase

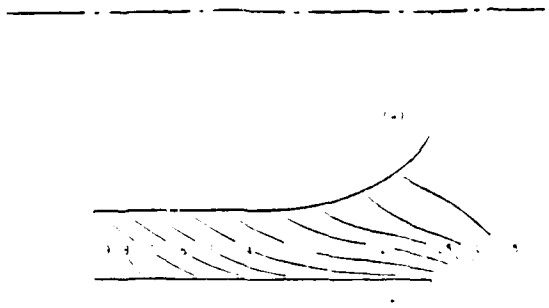

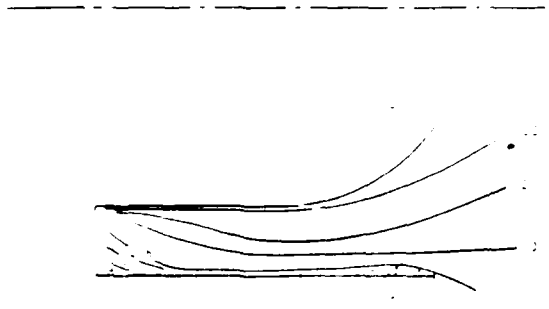

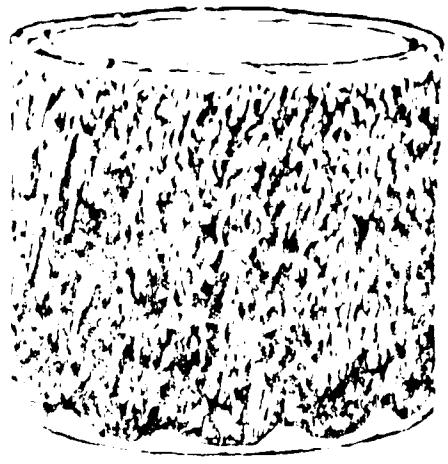

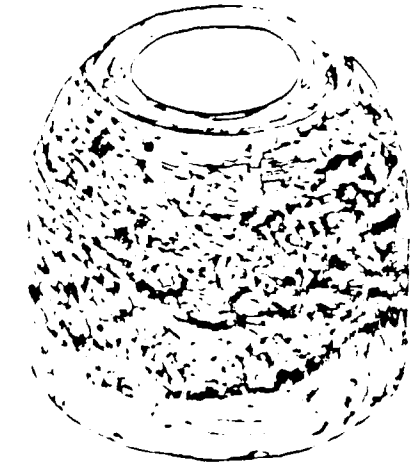

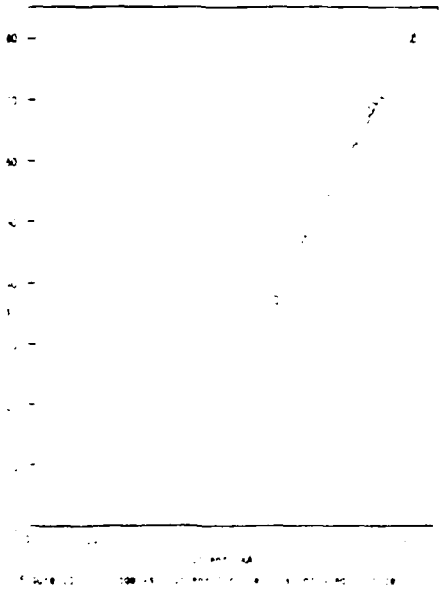

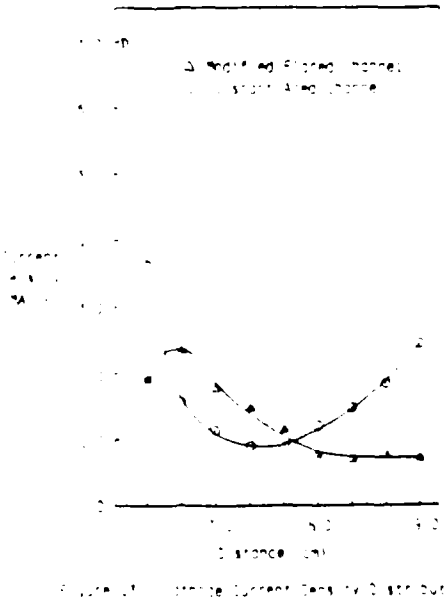

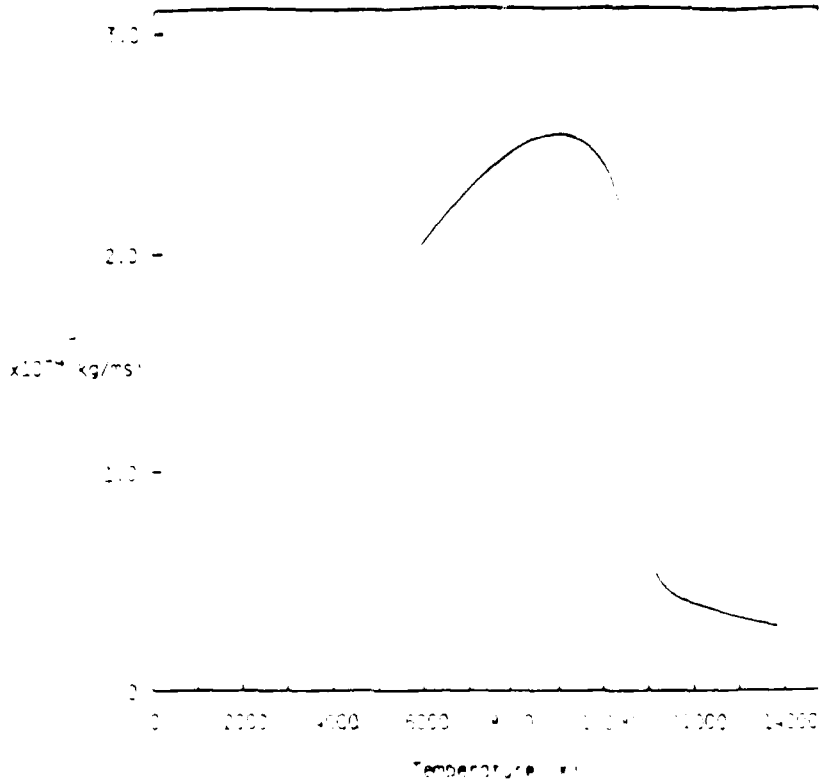

Figure 14: Viscosity of an Equilibrium Argon Plasma at 0.01 atm.

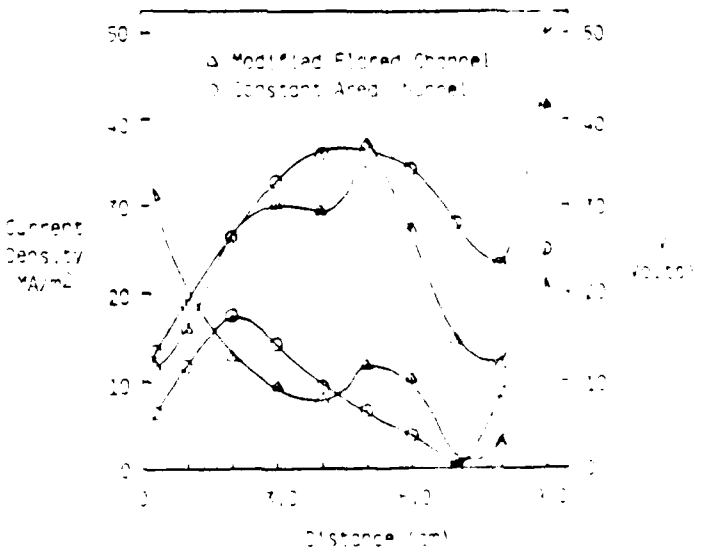

Figure 15: Distribution of Ion Temperature and Current Densities in Argon at 0.01 atm.

END

DATE

FILMED

DTIC

4/88